Characterization of Bio-Sensing Waveguides in CYTOP Operating with Long Range Surface Plasmon Polaritons (LRSPP's)

By

Asad Khan

A thesis submitted to the faculty of Graduate and Post-Doctoral Studies in partial fulfilment of the requirements for the degree of Masters of Applied Science in Biomedical Engineering.

15/10/2012

uOttawa

L'Université canadienne
Canada's university

School of Information Technology and Engineering (SITE)
University of Ottawa
Ottawa, ON, Canada

Acknowledgements

First and foremost I thank God for helping me in my pursuit of receiving higher education. I would like to thank my parents and the rest of my family for their endless support, patience and guidance throughout the years it took me to reach my academic goals. I would like to thank all contributors to my thesis particularly my thesis supervisor, Dr. Pierre Berini for his direction and encouragement as well as for providing me an opportunity to work within his group alongside other esteemed team members. I would also like to extend my gratitude to him and the University of Ottawa for allowing me the use of their labs and facilities to carry out the work described herein.

I would also like to deliver many thanks to my laboratory supervisor, Ewa Lisicka for all her help and mentorship and thank my colleagues, Alex Krupin, Fan Hui, Tony Olivieri, Michal Tencer, Charles Chiu and Hamoudi Asiri, for their assistance and making my stay at the University of Ottawa, a delightful experience.

Abstract

This thesis report works on optically characterizing waveguide based biosensors consisting of thin, narrow Au stripes embedded in CYTOP. The devices were examined using an ever evolving and improving interrogation setup, variations of which are described in detail in this document. A number of changes were made to the setup configuration in order to reduce noise levels and increase efficiency and accuracy of acquired measurements. Waveguides of varying configurations (straight waveguides and Mach-Zehnder Interferometers with etched and cladded channels) are described and optically characterized. The characterization results of these devices are presented in this thesis. Bulk index measurements are carried out in order to determine a suitable bio-sensing solution with a refractive index matched to that of CYTOP. Step index measurements clearly distinguishing the introduction of sensing solutions of refractive indices varying from one another, are made available. Preliminary bio-sensing experiments involving detection of change in refractive index of sensing fluid as well as adlayer thickness with the introduction of analytes binding to the waveguide surface that has been functionalized with antibodies, using both straight and cladded waveguides with single mode outputs are studied.

Contents

1. Introduction 1
1.1 Motivation: 1
1.2 Optical Biosensors 3
1.3 LRSPP Biosensors 7
1.4 Thesis Objective and Organization: 17
1.5 Thesis Contributions: 19
2. Device Structure and Design: 21
2.1 Device Structure: 21
3. Interrogation Setup: 27
3.1 Basic Setup: 27
3.2 Setup Design: 29
3.2.1: Setup Design 1: 29
3.2.2 Setup Design 2: 33
3.2.3. Setup Design 3: 34
3.3. DUT Mounting Jig: 36
3.3.1 Jig Design 1: 36
3.3.2. Jig Design 2: 39
3.3.3. Jig Design 3: 43
4. Setup Stability: 46
4.1 Stability Testing: 47
5. Bulk Sensing Measurements: 50
5.1. Overview: 50
5.2 Metricon Validation: 51
5.3. Bulk Sensing Measurements: 53
6. Device characterization results 58
6.1. Un-cladded Waveguides: 60
6.2 Cladded Waveguides: 61
6.3. Cladded waveguides with liquid filled etched channels: 65
6.4. Analysis: 70
6.4.1. Wafer CT-5 70
6.4.2. Wafers CWS 19 & CWS 24 71

6.4.3. Wafer CLT-13 71
6.4.4. Wafers ND I & ND II 72
6.4.5. Wafer CWS 24 72
6.4.6. Wafer At-Au-1 73
7. MZI Characterization Results: 74
8. Surface Biosensing: 82
9. Conclusions and Future Work: 86
10. References: 90

1. Introduction

1.1 Motivation:

Lung cancer and leukemia (blood/bone marrow cancer) are among the most common and most lethal of cancers worldwide. According to a study lead by World Health Organization (WHO), lung cancer was reported to be the most common cancer reported worldwide for several decades. By 2008, there was an estimated 1.61 million new cases of lung cancer reported worldwide making it 12.7% of the overall cancers reported. The mortality rate is also high with 1.38 million deaths reported attributed to lung cancer. Leukemia is another form of cancer which has caused a number of fatalities over the years. In the year 2000 alone, nearly 256,000 cases of leukemia were reported worldwide out of which 209,000 proved to be fatal [1].

Existing methods of detection rely mostly on imaging tools such as MRI's and CT scans used to detect the presence of tumours which is often at a stage where it requires invasive biopsy to determine its nature and further treatment strategy. More often than not, the imaging techniques discover the presence of cancer when it has already reached an advanced stage. Even worse, in some cases, the symptoms exhibited by a patient do not indicate the presence of cancer and the detection occurs 'accidently'.

There is thus a need for a diagnostics platform which is capable of detecting leukemia and lung cancer at an early stage before it metastasizes and spreads to nearby tissue and other parts of the body. This thesis was supported by BiopSys, an NSERC strategic network which aims at advancing plasmonic approaches for early cancer detection. A goal of this thesis is to discover new

methods and techniques that will exceed the performance characteristics of the current state of the art plasmon-based sensing technologies.

Numerous schemes for biosensing employing electrical, mechanical or thermal means have been explored in the past. Electrochemical impedance measurements have been used to detect the presence of analytes in [2]. Similarly, thermoelectric thermostats have been employed in studies to detect the presence of a specific ingredient caused by the activation of a special enzyme reaction generating heat [3]. However, this thesis discusses an optical method as the means for interrogation in a biosensor, to detect and distinguish biological samples.

A conventional biosensor consists of florescent probes used to tag specific targets [4]. When illuminated with light, the probes fluoresce indicating the presence of the target analyte. This technique, though useful and extremely sensitive, with a detection limit down to a single molecule [5], is plagued with limitations such as photo bleaching which renders the probes useless over time as they stop emitting light after repeated exposure to light. The process of labelling the sample is also time-consuming, laborious and may sometimes interfere with molecular interactions. Fluorescence signal bias can also cause quantitative analysis to become a challenging process as the number of fluorophores on each molecule cannot be precisely controlled [6].Due to these limitations, techniques which allow label-free, direct sensing are highly sought after. As the name suggests, target molecules need not be labeled or altered by any means and is thus easier and cheaper to perform. Unlike fluorescent tagging, the label-free strategy also allows for quantitative molecular interactions. Numerous electrical, electrochemical, mass sensitive, thermal and optical approaches have been employed to design transducers to address this need [7].

A need to move towards label-free detection schemes which allow for reduced detection time as well as direct sensing is currently addressed by the commercially available Surface Plasmon

Resonance (SPR) based platforms. A vast majority of current optical means for biosensing are based on surface plasmon resonance, the most widely popular approach being the Kretschmann-Raether geometry [8]. The technique has dominated the biosensor market for numerous years but despite making a substantial contribution in the field of biosensing, there hasn't been significant improvements in the in the technology over the years. Despite their popularity however, these devices too, are susceptible to attenuation.

Long Range Surface Plasmon Polariton (LRSPP) based biosensors not only rectify the propagation losses associated with SPR but also allow for finite metal strip configurations which can be modified to create a number of useful integrated geometries (S-bends, Mach-Zehnder interferometers etc).

1.2 Optical Biosensors

A biosensor is a device used to detect and analyze the biochemical substances present in a given sample. It allows for the conversion of a chemical reaction into a signal which can be measured and manipulated to acquire useful information like concentration, composition, function and various other biochemical parameters of interest. With the rapid advances in the field of biomedical instrumentation, health care officials are increasingly reliant on testing and identification platforms which are cheap, accurate, fast and user friendly. A general schematic of a biosensor would consist of recognition elements such as enzymes, proteins, antibodies etc, designed to target a certain molecule of interest, interfaced with a transducer which then converts and reports a measureable response (see figure 1).

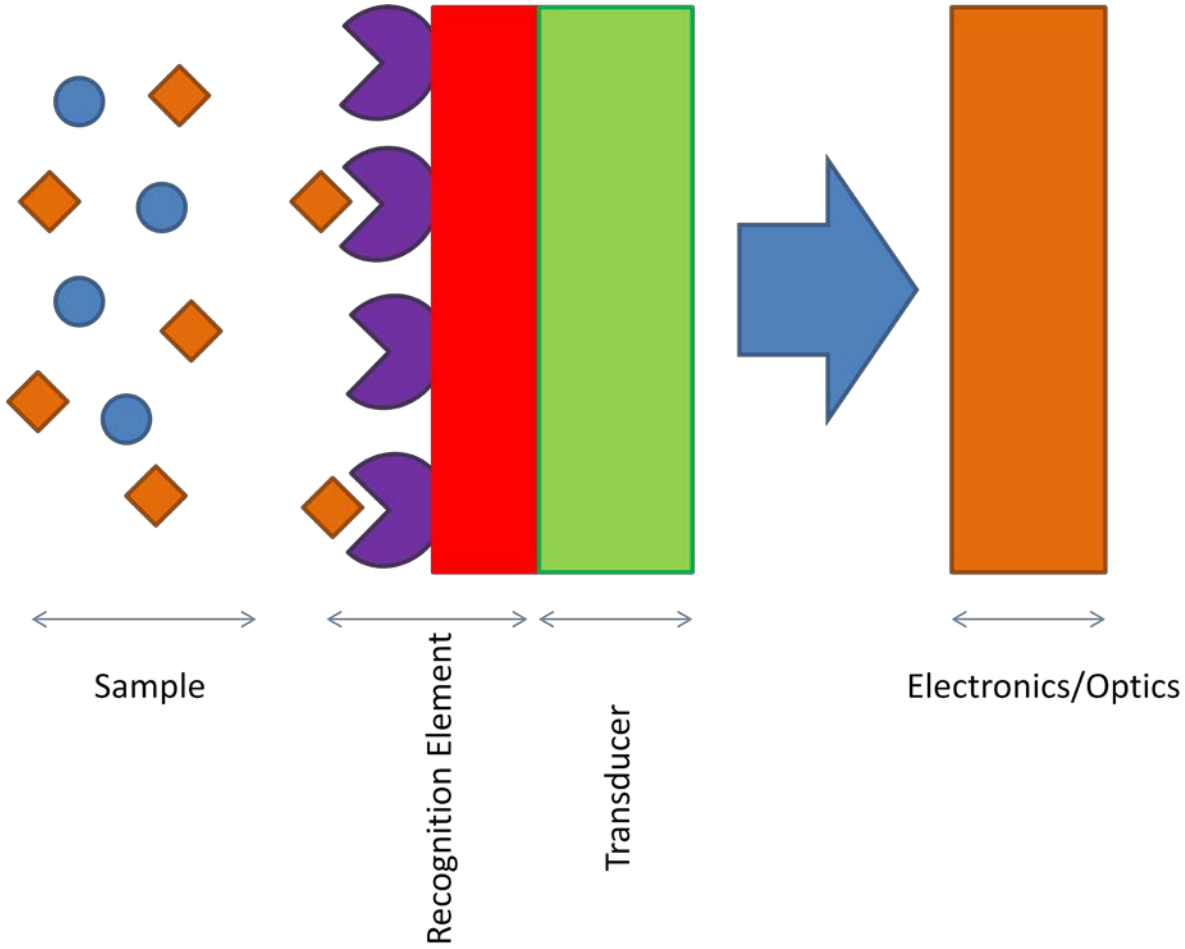

Figure 1: A schematic of a typical biosensor illustrating the sensing element, a transducer and associated electronics/optics to measure response.

Optical biosensing platforms are promising for the biomedical, health care and pharmaceutical sectors, and for environmental monitoring, homeland security and the battlefield; by proving themselves capable tools for detection and analysis [9,10]. They have also been found useful by proving immune to electromagnetic interference, demonstrating capability of performing remote sensing and providing multiplexed detection with a single device.

The biosensing approach utilized for this study as well as one of the approaches being widely adopted today for fast and simple determination of clinical, biochemical and environmental analytes is that of an immunoassay sensor that relies on antibody-antigen interations. This interaction forms the basis for a sensing platform that is very promising owing to both its specifity and sensitivity. Specificity relies on recognition of target analytes by antibodies, forming a stable complex on the surface of an immunoassay sensor [11]. The sensitivity factor relies on factors such a high affinity, analyte specific antibodies, their orientation after being immobilised on the sensing surface and the detection system for measuring the analytical signal [11]. Optical means are utilized to measure the response signal which in this case happens to be the change in refractive index which occurs when a target molecule binds to an antibody over time.

Figure 2 illustrates a platform of interest consisting of planar gold waveguides. Gold is the metal of choice for biosensing applications for a number of reasons. A good quality thin gold film with low surface roughness, allows easy self-assembled monolayer (SAM) formation, which in turn helps analyte/receptor interactions. Thin films of gold can be readily deposited by means of physical vapor deposition, sputtering or electro-deposition. A number of lithographic techniques are available and understood well enough to pattern gold easily. The metal is inert for the most part and hence doesn't react with most chemical compounds. It is also biocompatible with cells and other living organisms allowing them to bind to its surface without proving toxic [11]. Other metals such as silver, though known for their use in metal deposition applications, are seldom used for biosensing applications due to cell toxicity and their reactive nature.

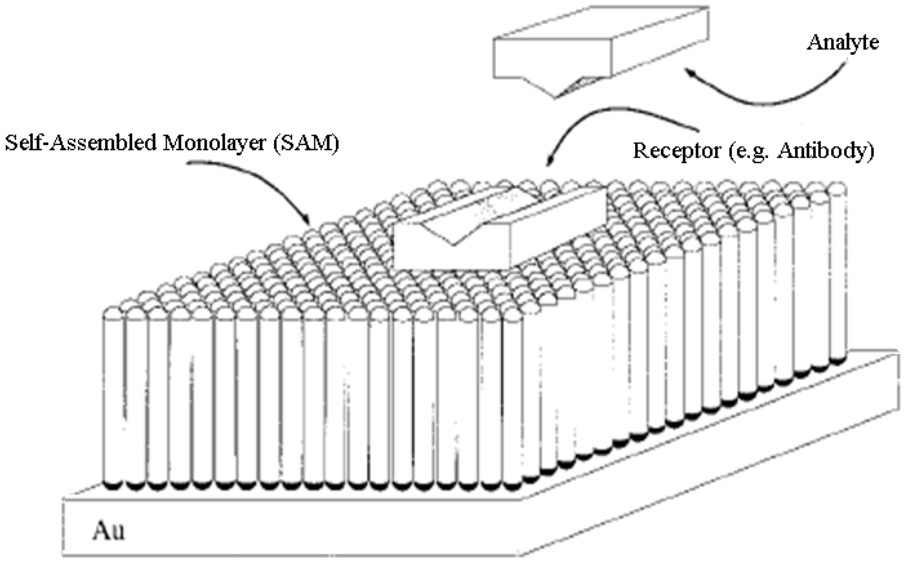

Figure 2: Surface functionalization of gold facilitating analyte receptor binding for optical bio-sensing applications. Adapted from [12].

Self-assembled monolayers (SAMs) of thiols on metals and semiconductors are widely popular organic molecular films [13], [14]. Thiol SAMs form an easy pathway to link inorganic, organic and biological materials of interest, to metal surfaces [15]. The sulfur atom of the molecule links a hydrocarbon chain of variable length to the metal surface through a covalent bond, while van der Waals forces between neighboring molecules contribute towards stabilizing the structure [12]. The terminal group of the SAM can either block or promote protein adsorbtion [15]. This useful property can be utilize to selectively functionalize various surfaces. The details of selective functionalization as well as steps leading to surface preparation for biosensing can be found in [12]. Here it is important to note that most of the surface chemistry on the biosensors was done by other students and technical staff at the University of Ottawa.

1.3 LRSPP Biosensors

The phenomenon of surface plasmons was first observed in 1902 by Wood who shone polarized light through a mirror with a diffraction grating on its surface. The result was a pattern of dark and light bands in the reflected light [16], [17]. Further interpretation of this was discussed by Fano in 1941[18]. The most elaborate and complete explanation however was not given until Otto, Kretchmann and Raether came along in 1968[19], [20]. It is now known that coherent electron oscillations exist at the interface of a metal and a dielectric, in other words, materials whose real part of the dielectric function is positive on one side and negative on the other side of the material boundary (see figure 3 a and b). These oscillations, when excited by an external source such as a photon, incident at a specific angle, fuse with the electron oscillations forming a hybrid, self-sustaining excitation called a surface plasmon polariton or SPP.

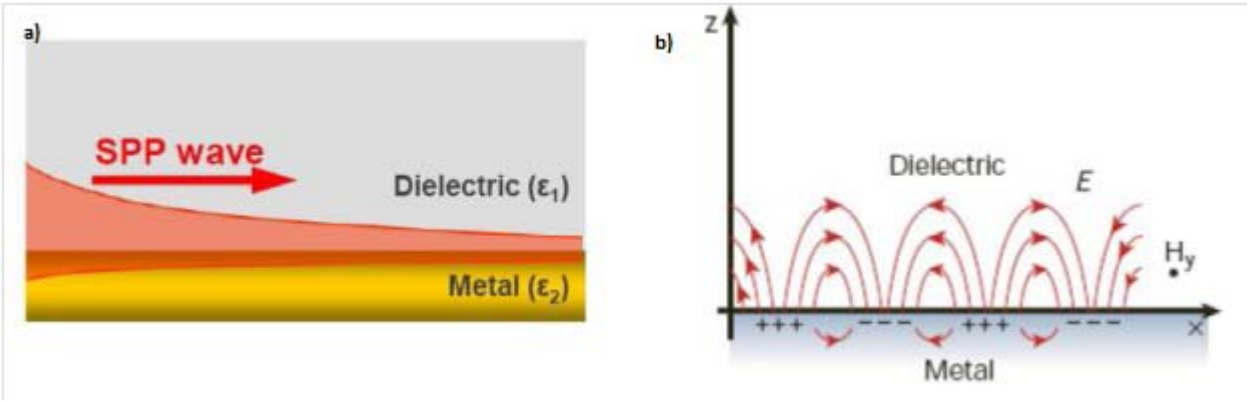

Figure 3: (a) Surface plasmon propagation at metal-dielectric interface. (b) Oscillations in surface charge density and electric field lines. Adapted from [11].

The true nature of surface plasmon polaritons is best understood by utilizing Maxwell's equations to the simplest possible geometry capable of sustaining SPP's i.e. a metal-dielectric interface (see figure 4). To describe the behaviour of the free electrons present at the metal dielectric interface, Drude's model for a free electron gas is employed, which is similar to the Lorentz harmonic-oscillator model except that it negates the spring constant effectively eliminating the binding force between the electrons and the nucleus. This gives rise to the SPP wave vector (k_{sp}) which relies on the permittivity of both the metal ($\varepsilon_{r,M}$) and that of the dielectric ($\varepsilon_{r,D}$). For any given excitation wavelength, there is only one specific wave vector. It is important to remember that the modes excited at a metal-dielectric interface are TM modes since TE modes do not allow opposite signs of permittivity for the mediums in contact (metal and dielectric) which have opposing permittivity.

Figure 4: The above figure demonstrates the field strength distribution for a single interface SPP.

The discovery of Surface Plasmon Resonance (SPR) has paved the way for optical transduction methods to gather momentum in the field of biosensing. The most popular and readily

available approach towards realizing the potential of SPR in a commerical biosensing schemes is a biosensor by BIACORE [21], [22]. The BIACORE sensor is based on the Kretschmann prism configuration where a glass prism is used to excite surface plasmons at a metal-dielectric interface. A thin semi-transparent metal layer (usually a noble metal) is deposited on one of the faces of a prism such that the conditions for total internal reflection (TIR) are facilitated at the metal-dielectric interface. The phenomemon of TIR will cease to occur once the incident angle decrease to the critical angle (Θ_c). At the critical angle, some of the light escapes and is refracted across the interface causing an evanescent field to penetrate the second interface where coupling to SPPs may occur.

As briefly mentioned earlier, the phenomenon of SPR is only observed at a certain incident angle when the light is p (TM) polarized and where the incident wave vector is given by the following expression:

$$K_i = (^{2\pi}/_{\lambda)}\, n \,\mathrm{Sin}\, \theta_i \quad \text{- (Equation 1)}$$

where K_i represents the component of the incident light wave vector that is parallel to the prism interface, Θ_i represents the angle at which the light is incident, the wavelength of this light is given by λ and the refractive index of the prism is denoted by *n.* The wave vector of the plasmon mode can be written as follows:

$$K_{sp} = \left(^{2\pi}/_{\lambda}\right)\sqrt{\frac{\varepsilon_{r,M}\varepsilon_{r,D}}{\varepsilon_{r,M}+\varepsilon_{r,D}}} \qquad \text{- (Equation 2)}$$

where K_{sp} defines the surface plasmon wave vector and the relative permittivity for the metal and the dielectric are given by $\varepsilon_{r,M}$ and $\varepsilon_{r,D}$, respectively. The phenomenon of SPR is witnessed when $K_i = K_{sp}$. The incident light, at a given coupling angle Θ, couples to the surface plasmons exciting the SPR wave and causing a drop in the intensity of the reflected beam. The coupling angle can change when an analyte solution is brought into contact with the metallic surface, prefunctionalized to bind with

the molecule to be sensed, via a target specific receptor. It is this change in the angle which is monitored to detect biosensing events. This change in angle results due to the change in refractive index of the dielectric medium at the surface of the gold layer, through which the reflected light must travel.

Figure 5. illustrates the popular Kretschmann configuration with the EM field peaking at the metal-dielectric interface and decaying sharply within a fraction of a wavelength which is referred to as an 'evanescent field [23]. The Kretschmann sensor affords high sensitivity and a low detection limit [2] where the accumulation of biofilms on the gold layer as a result of molecules binding to affinity ligands, can trigger a detectable response due to a change in refractive index.

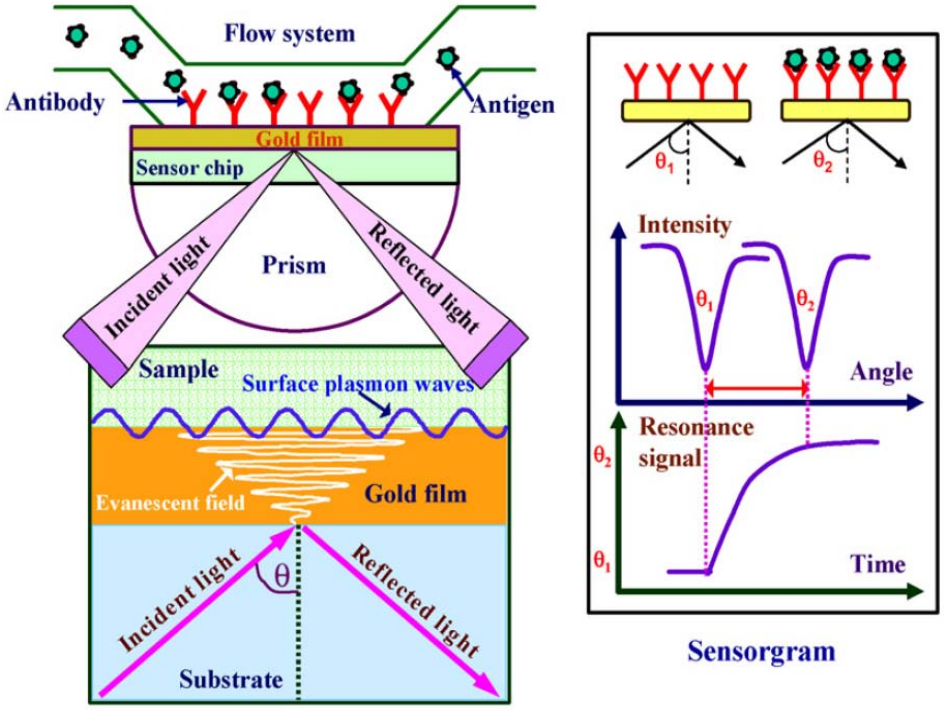

Figure 5: The Kretschmann configuration where a prism is used to couple incident light into a metal-dielectric interface. Adapted from [24].

SPR based sensors can be further improved upon by enhancing their sensitivity which can be achieved by various means. Some of which include incorporating bimetalic layers [25] and

gratings [26], [27]. The strategy of particular interest in this study incorporates the use of Long Range Surface Plasmon Polaritons (LRSPPs) for interrogating biosensors constructed out of insulator-metal-insulator waveguides (see figure 6). With the advances in planar waveguide fabrication techniques and their existing mass deployment in the communication industry already using integrated waveguides as biosensing platforms is practical. Transducers based on integrated planar waveguides utilize evanescent field sensing (EFS) which peaks within the core and decays away into the surrounding cladding. The propagation constants can be varied by using appropriate bulk or thin layer claddings around the waveguide[28].

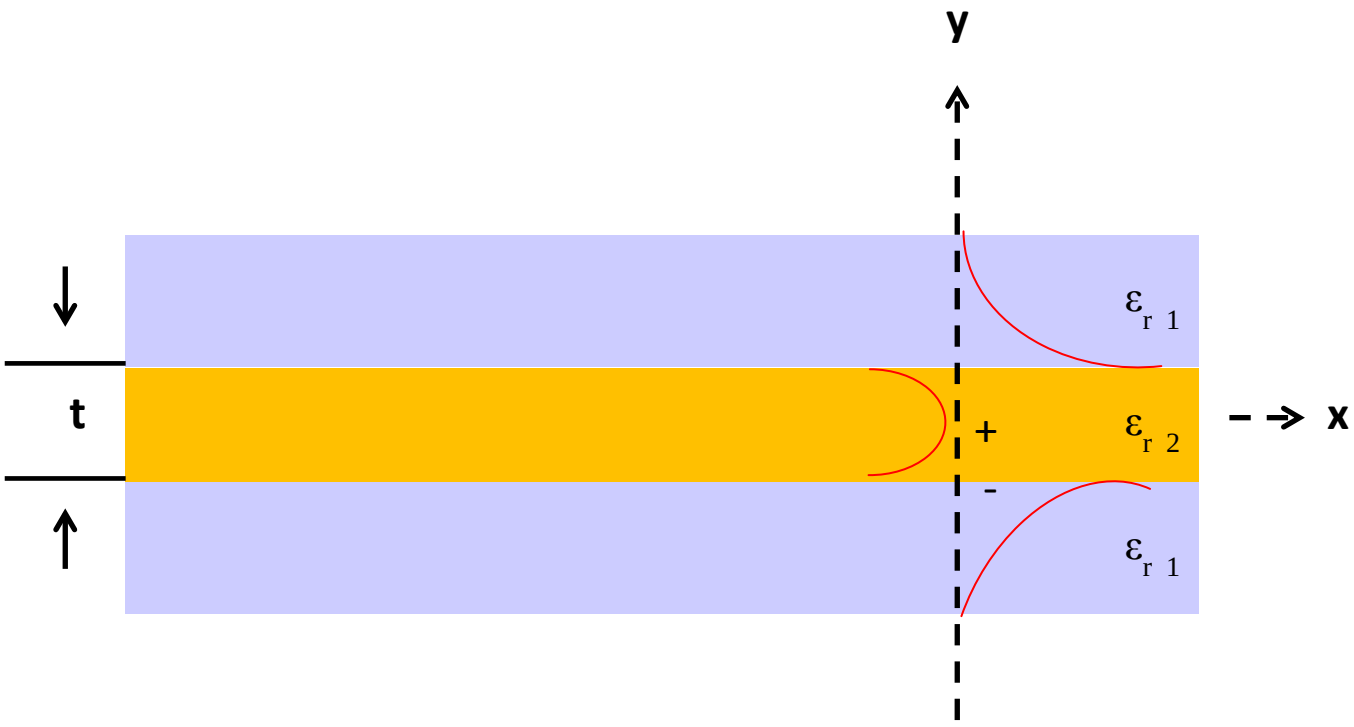

Figure 6: The above figure demonstrates the field strength distribution for a symmetrically cladded LRSPP bound on both sides by same dielectric medium with a matching refractive index.

By bounding a thin metal film of a particular thickness ***t*** on both sides by a dielectric medium of the same refractive index ($n_1 = n_2$), two single interface SPPs couple to form symmetric (***s_b***) and asymmetric (***a_b***) supermodes (where the suffix 'b' stands for bound). Of the two, the symmetric mode is known to propagate distances which are up to 2 orders of magnitude longer than what the single interface SPP's are known to travel and are hence known as LRSPPs [29].

One of the key findings reported in this document are characterization results of metal stripe waveguide based biosensors. The fabrication process evolved and improved over time in order to ensure development of high quality waveguide structures that adhered to the theoretical recommendations and complied with guidelines illustrated in earlier studies. It was determined that the slab geometry with finite width dimensions, is the preferred configuration for realizing metal waveguide platforms[33] (see figure 7). This method allows construction of stripe waveguide structures capable of supporting the following four 1st order modes:

- Symmetric-symmetric bound (ss^0_b).
- Symmetric-asymmetric bound (sa^0_b).
- Asymmetric-symmetric bound (as^0_b).
- Asymmetric-asymmetric bound (aa^0_b).

For LRSPP applications, it is the ss^0_b mode, that is of prime interest due to its low propagation attenuation constant compared to the single-interface SPP mode counterpart and it can be isolated from the rest by simply reducing the thickness of the metal. This is due to the cutoff thickness associated with the fundamental and higher order modes below which they no longer propagate.

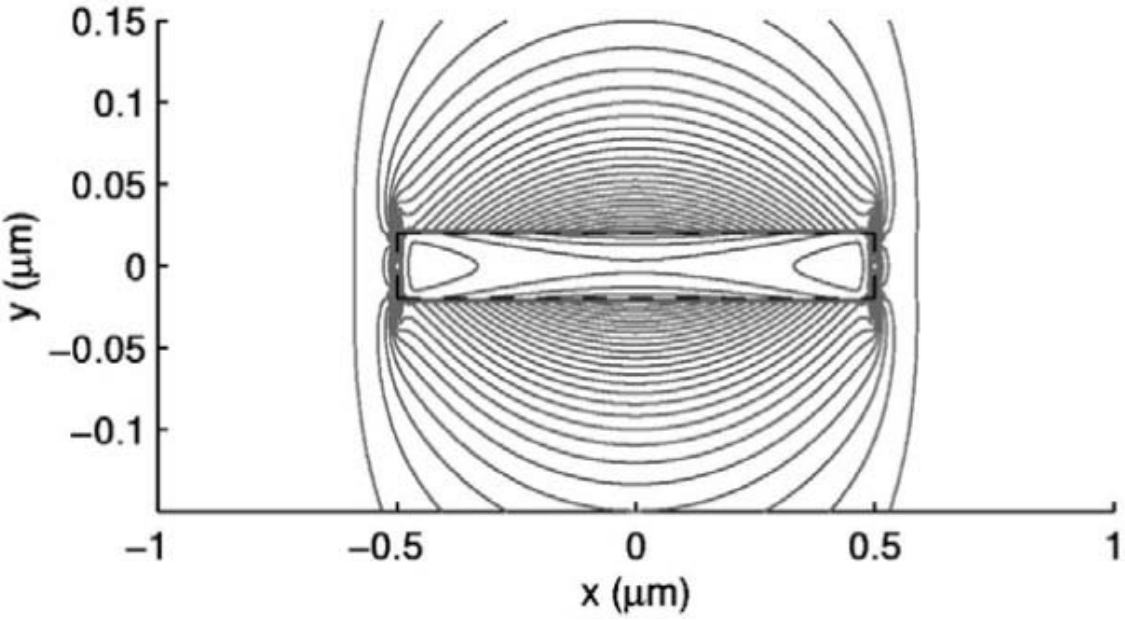

Figure 7: Stripe waveguide structure with finite width to support the fundamental LRSPP mode. Adapted from [28].

This is the main reason why symmetrically cladded Au waveguides in dielectric material, form the basis of the structures studied in this document. An asymmetric structure would have a metal layer bounded on both sides by a dielectric medium of different permittivities. This type of structure, though capable of sustaining the ss^0_b mode, causes the mode to have a higher attenuation constant compared to its counterpart excited in a symmetric structure [28] (figure 8) where thickness of the structure is plotted against the propagation constants associated with both symmetric and asymmetric structures. A higher attenuation constant can affect the performance of the sensor by reducing its sensitivity [8].

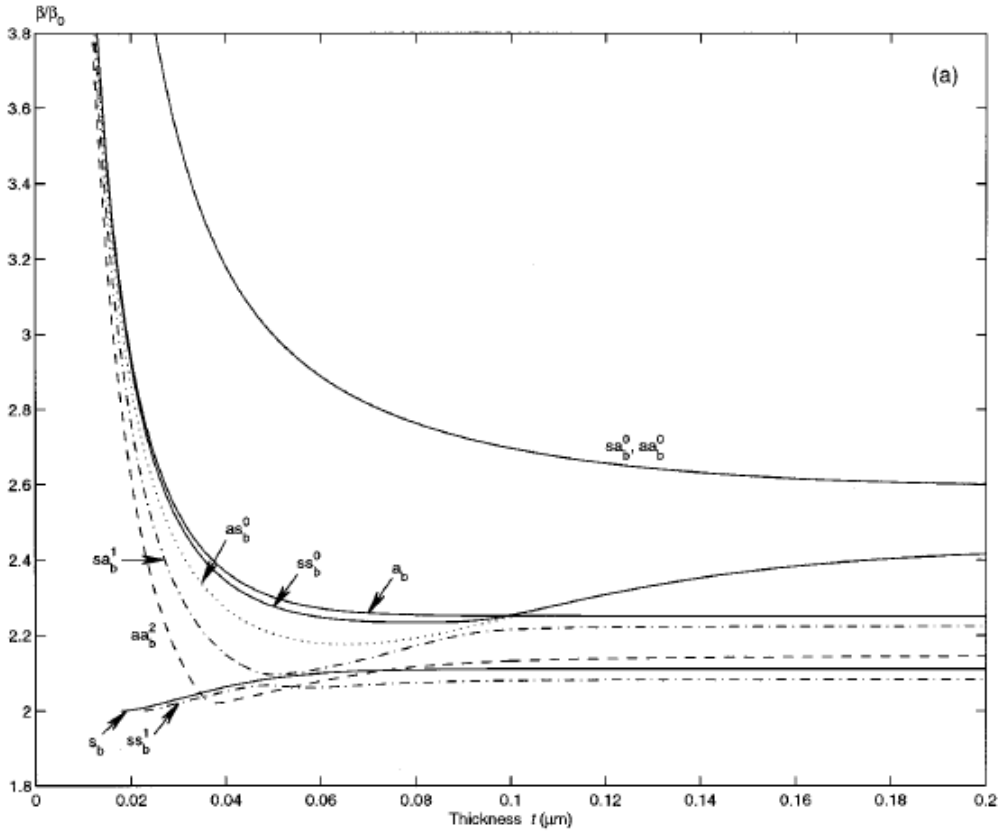
β/β0
(a)
sa0b, aa0b
as0b
ss0b
ab
sa1b
aa2b
sb
ss1b
Thickness t (μm)

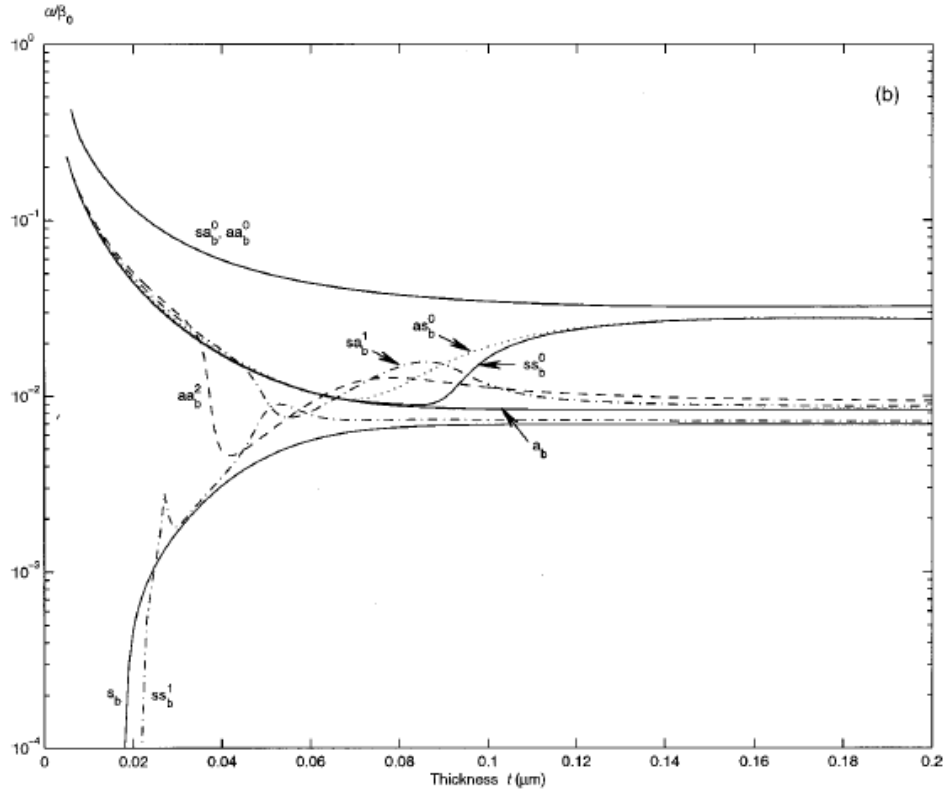
α/β0
(b)
ss0b, aa0b
as0b
sa1b
ss0b
aa2b
ab
sb
ss1b
Thickness t (μm)

Figure 8: Mode attenuation constants versus stripe metal thickness (a) symmetric structure (b) asymmetric structure. Adapted from [28]

A Mach-Zehnder interferometer (MZI) geometry can be employed with Evanescent Field Sensing (EFS) based waveguides, to take advantage of the dual arm layout where one arm acts as the reference arm while the other serves the purpose of the sensing arm [29], [30]. In a typical biosensing experiment utilizing a MZI would involve functionalization of the sensing arm with a recognition element associated with the target analyte such that when a carrier solution with a particular analyte is washed over the waveguide, analyte binds to and is immobilized on the surface (see figure 9). A variation in power caused by a varying phase difference between the arms can be measured via the output end of the MZI which serves as an indication of the presence of the target.

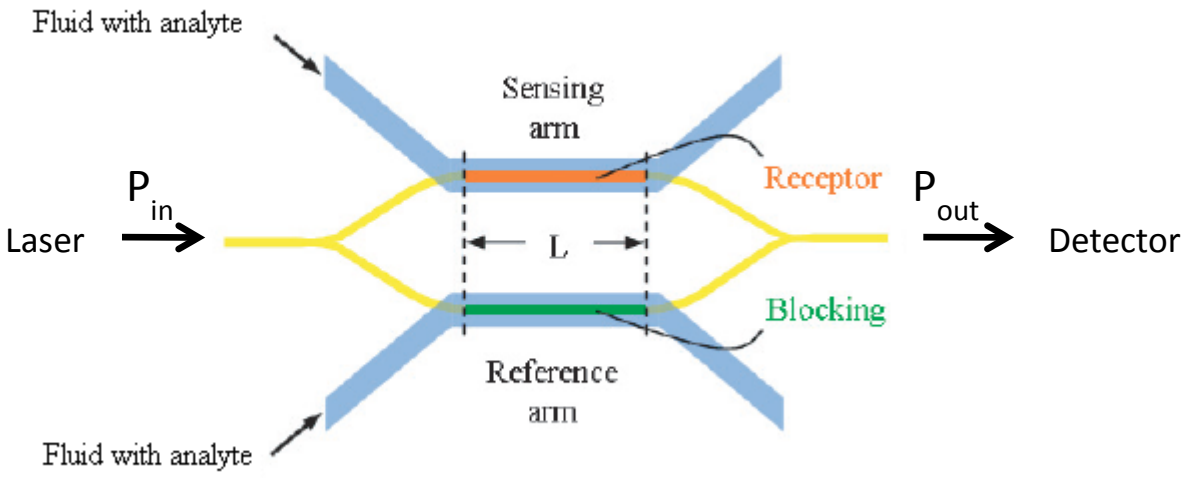

Figure 9: MZI demonstration for surface sensing with sensing and reference arms. Adapted from [8].

The thin metal film bounded by dielectric media on both sides is useful in this case where if a thin adlayer of a different refractive index is added on to the gold surface (see figure 10) it raises the attenuation constant thereby stunting the propagation distance of the mode. This is readily observed as a decrease in the optical power output of a straight gold waveguide. Similarly, a MZI configuration can be utilized to measure changes in wave intensity, which ultimately is an indicator of decreased wave velocity also caused by the adlayer [31].

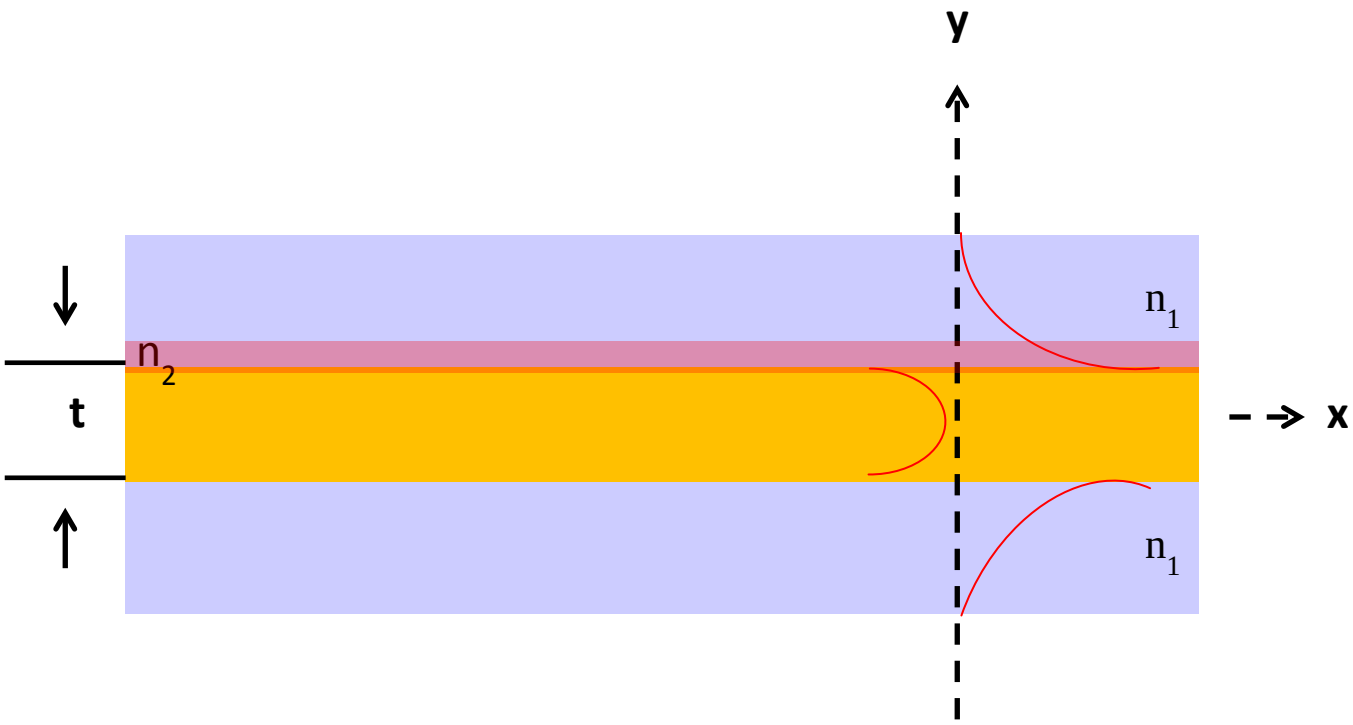

Figure 10: The above figure demonstrates presence of an adlayer on gold with a different refractive index then that of the dielectric material surrounding the gold layer.

It is thus a logical conclusion that the sensitivity of the sensor can be enhanced by lowering the attenuation constant such that longer optical interaction length structures can be used. In [8], the surface and bulk sensitivities of the MZI sensor are studied. It is reported that surface sensitivity of the MZI structure is dependent on the length of the sensing arm of the MZI. Higher sensitivity can be achieved by increasing the length of the sensing arm on the MZI, provided that the waveguide is

lossless, an ideal scenario. In practice however, the length of the waveguide is limited by the attenuation constant. Lowering the attenuation constant, therefore, is highly desirable and is very much reliant on the quality of the biosensor. By executing a carefully designed fabrication process, devices consisting of waveguides with sharper resolution, gold surfaces with minimal aberrations, reduced surface roughness and minimal waveguide deformation can be achieved [32].

1.4 Thesis Objective and Organization:

The main objective of this study is to evaluate Long Range Surface Plasmon Polaritons as means for probing and optically interrogating waveguides which are chemically functionalized to attach to analytes and thus act as optical biosensors for detection as well as identification of cells based on cell identity markers.

A large portion of this thesis is dedicated towards interrogating waveguides fabricated out of Au embedded in CYTOP (a carefully chosen cladding material such that it is index matched to the sensing transport fluid) which are characterized for eventual biosensing experimentations employing Long Range Surface Plasmon Polaritons (LRSPP's). However, there are several preliminary steps which lead up to the optical testing of devices. This thesis is divided into a number of sections, each exploring some of the major and minor goals organized in a chronological order for ease of understanding. A brief chapter summary of this thesis is presented below:

Chapter 2 – Device Structure and Design:

This chapter is a brief overview of the devices under test as candidates for an optical biosensing platform. The device geometry, etch patterns, device fabrication and layer by layer analysis are given.

Chapter 3 – Interrogation Setup:

This chapter includes the experimental setup design and evolution over the span of the study. It's an in depth description of varying setup layouts and jig designs which were devised over time to interrogate several generations of optical waveguides and devices of varying forms.

Chapter 4 – Setup Stability:

The emphasis of this chapter is to highlight the importance of setup stability during optical interrogation. Varying setup configurations discussed in the preceding chapter, are compared here.

Chapter 5 – Bulk Sensing Measurements:

The importance of index matching is highlighted in this chapter. A number of solutions with varying refractive indices are examined to determine one that is ideally matched to the refractive index of CYTOP. Step index measurements are also presented to demonstrate the sensitive nature of the devices.

Chapter 6: Device Characterization Results:

This chapter is an in-depth study of devices procured from a number of fabrication batches consisting of various device layouts and representing changes made to the devices in an effort to improve their performance.

Chapter 7: MZI Characterization Results:

Sensing results from a single output MZI with side access fluidic channels are presented in this chapter. Experimental results are compared against theoretical values.

Chapter 8: Surface Biosensing:

A short experiment conducted to validate the ability of the sensor to detect bacteria, is detailed in this chapter.

A concluding chapter ties everything together by summarizing the objectives of the thesis as well as with recommendations for work that could be carried out in the future to take the efforts made so far and improve upon them further.

1.5 Thesis Contributions:

This thesis lays the foundation for optical device testing by pulling together an interrogation setup which enables a probing fiber to excite an optical mode. Several variations in the setup layout were explored in this thesis with the merits and limitations of each discussed. The evolution of setup layouts took place to keep up with the dynamic nature of the devices which changed and improved over time. The jig used to house the device during optical interrogation, was also altered to accommodate the changing devices as well as to integrate a number of requirements, some of which included (but were not limited to): easy access of fiber to the device, circulation of index matching fluid through the device and easy visual inspection of device during testing etc. The stability of the setup was also improved upon to increase the credibility of the measurements obtained by minimising noise from the measured optical signal. Solutions of varying refractive indices and their effect on the output of the signal were also demonstrated in this thesis. Devices of varying nature (with differing cladding / waveguide thicknesses, etched, cladded, with/without channels etc) were also tested and had their biosensing capabilities examined. A single output MZI was interrogated for the first time since this project began, with the results outlined in this thesis. The biosensing results presented in this thesis are also the first demonstrating the sensing capabilities of the device.

The multi-disciplinary nature of this project meant that a number of key contributions were made by a team of people invested in driving this project forward. The device layout and mask design work was carried out by Ewa Lisicka-Skrzek. The fabrication effort was put in by Charles Chiu, Reza Hanif and Hamoudi Asiri. Surface chemistry on the biosensors was done by Michal Tencer and Alex Krupin. Their contributions in this thesis were absolutely crucial.

Personal contributions were made to the following papers published during the span of this thesis research:

- Daviau, R., Khan, A., Lisicka-Skrzek, E., Tait, R. N., BERINI, P., "Fabrication of surface plasmon waveguides and integrated components on Cytop," (Elsevier) Microelectronic Engineering, Vol. 87, pp. 1914-1921, 2010.

- Asiri, H., Khan, A., Lisicka-Skrzek, E., Tait, R. N., BERINI, P., "Fabrication of Surface Plasmon Waveguides in Cytop," SPIE Photonics North: CIPI, Montréal, Canada, June 2012.

- Khan, A., Krupin, A., Lisicka-Skrzek, E., BERINI, P., "Sensing of bacteria immobilised under static conditions using long-range surface plasmon waveguides in Cytop," SPIE Photonics North, Ottawa, Canada, May 2011.

- Khan, A., Chiu, C., Lisicka-Skrzek, E., Tait, R. N., BERINI, P., "Characterization of Biosensing Waveguides on Cytop," SPIE Photonics North, Vol. 7750, 77500H, Niagara Falls, Canada, June 2010.

- Krupin, O., Khan, A., Wang, C., BERINI, P., "Long-Range Surface Plasmon Polariton (LRSPP) waveguides as a platform for blood group immunophenotyping," Nano-ONTARIO 2011 - Ontario Nanoscience and Nanotechnology Workshop, McMaster University, Hamilton, Canada, May 2011.

- Khan, A., Chiu, C., Lisicka-Skrzek, E., Tait, R. N., BERINI, P., "Characterization of Biosensing Waveguides on Cytop," NanoONTARIO 2010 - Ontario Nanoscience and Nanotechnology Workshop, University of Western Ontario, London, Canada, May 2010.

2. Device Structure and Design:

2.1 Device Structure:

This section describes the metal stripe waveguide platform chosen for carrying out biosensing experiments for the scope of this project. There are several reasons to use this waveguide geometry for label free biosensing, instead of using the conventional and popular SPR sensor based on the prism coupler approach. The metal stripe waveguide configuration affords lateral confinement and propagation of the long range surface plasmon mode with lower attenuation. The direct result of this is highly sensitive devices. The waveguide configuration also allows for a simpler and more efficient end-fire excitation approach from a fiber, for optical interrogation of the devices. Also a number of different integrated structures including MZI and straight waveguides can be constructed with ease due to well understood fabrication methods.

As discussed in the previous section, for an optimal biosensing platform comprising of dielectric bounded metal waveguides, the goal is to reduce the attenuation constant. A requirement to achieve that is to ensure that the dielectric materials cladding the thin metal layer have the same permittivity. This will ensure a perfectly symmetric LRSPP compatible device. Furthermore, in choosing the cladding material, care must be taken to select a polymer to ensure that it is index matched to the bio-sensing fluid which will form the top cladding in cases where an etched channel with an embedded waveguide is filled with the solution. A refractive index mismatch between the bottom cladding of the device and the analyte solution used to fill the etched micro fluidic channels would result in an asymmetric device with decreased sensitivity.

In this study, the material used for the fabrication of planar devices forming the structurally symmetrical upper and lower claddings of the devices is a fluoro-polymer known as CYTOP. It has a

known refractive index of 1.33 at λ = 1310 nm, which is close to that of de-ionized water; very suitable for biosensing applications. Aside from fulfilling the key requirement of index matching, CYTOP is also the dielectric material of choice for the fabrication of the planar devices discussed in this document, for several other reasons. It is found to be impervious to water, oil and several other chemicals (with exception to a fluorocarbon solvent used for dissolving it). It can also be applied easily to a silicon wafer by means of spin coating, dip coating and potting [11].

The devices studied and characterized in this document consisted of gold waveguides, fully embedded in CYTOP, fully etched gold waveguides immersed in index matched fluid/oil, partially cladded straight waveguides (with an etched micro fluidic channel for index matched sensing fluid) for selective exposure of sensing surface, and fully/partially cladded MZIs (with a cladded reference arm and an etched sensing arm). The gold waveguides demonstrated in the figure 11 below are 5 µm wide and 35 nm thick. The thickness of the CYTOP layers forming the top and the bottom cladding varies between 8-9 µm (from one batch of wafer to the next).

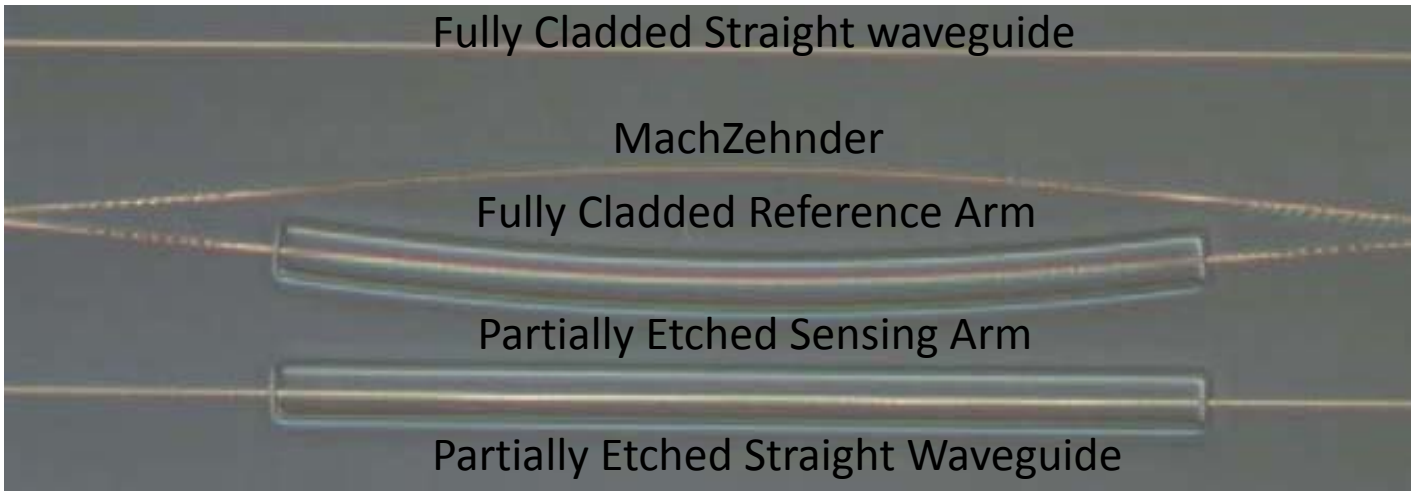

Figure 11: Stripe waveguide based biosensing structures with fully cladded and partially cladded straight waveguides and a MZI with an etched sensing and cladded reference arm.

As demonstrated in figure 12 which follows, the micro fluidic channels etched on the devices to expose them to the sensing fluid measure 80 µm wide and 8 µm deep, with a slight over etch beyond the waveguide level. This is to ensure and facilitate the full exposure of the waveguides to the sensing fluid carrying the biological entity being detected [11].

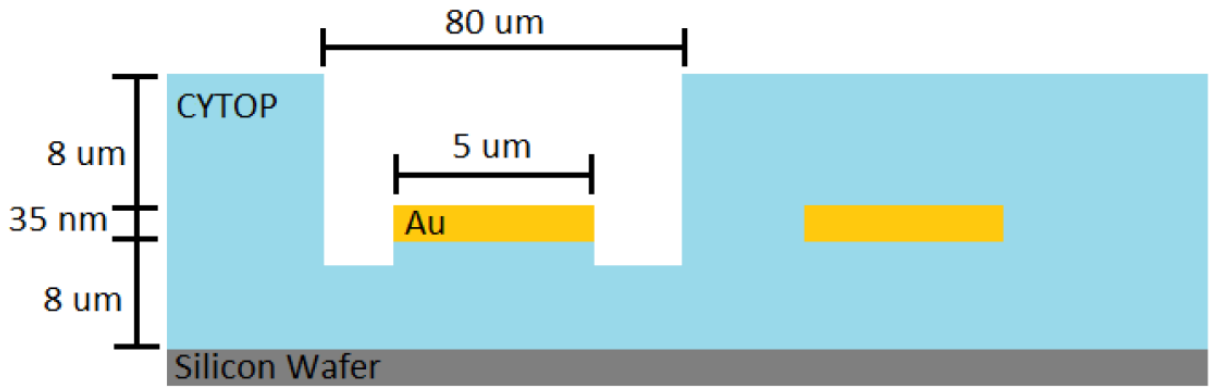

Figure 12: Device schematic with dimensions for channels and waveguides. Adapted from [11].

The devices tested and reviewed in the initial phases of this project and the ones tested near the end of the project, came from two separate students taking part in the ongoing project. Each of them made various contributions to the fabrication process and steadily improved the quality of the wafers coming out the fabrication laboratory located at Carleton University, Ottawa. Despite the improvements in feature resolution and surface roughness of the devices, by means of tweaks incorporated in the fabrication process, the underlying steps that form the basis of the device manufacture remain the same. The fabrication process can divided into two separate levels namely device level and channel level.

The device level consists of steps leading up to the deposition of gold waveguides onto the Si substrate wafers clad in CYTOP. The channel level consists of selectively etching fluidic cavities over the waveguides.

At the device level, the process begins with priming of the wafer which requires cleaning the wafer, preparing it for spin coating of multiple layers of CYTOP which form the bottom cladding of the devices on the wafer. A number of CYTOP layers were spin coated on the wafer in order to obtain enhanced adhesion between layers and to prevent the buildup of moisture between layers which can affect the structural integrity of the waveguides.

Once the silicon substrate is coated in CYTOP forming the bottom layer for the metal devices, the wafer is ready for bi-layer lithography; a process which is utilized to deposit metal devices onto the substrate. The process is dubbed 'bi-layer' lithography because at this stage, the devices are coated with a layer of lift-off resist and a layer of photo-resist. The two layers are then selectively etched to pattern the substrate for metal deposition which follows.

Gold has to be deposited immediately following the lithography of the patterns. The timing is important in an effort to keep the wafers from getting contaminated. An electron beam metal evaporator was employed to deposit desired thickness of gold under vacuum. The deposition process was closely monitored to ensure that no power fluctuations during the deposition process caused the evaporator to sputter gold 'spits' on to the devices. Finally, after the gold deposition is complete, the device level fabrication process is concluded by immersing the wafer in a solution of resist stripper to wash off the previously deposited layers of lift-off resist and photo-resist from the wafer.

Once device level fabrication process is concluded, channel level fabrication can begin. This procedure entails patterning and then subsequent removal of CYTOP from the top cladding of waveguides via selective etching, leaving exposed gold waveguides for fluidic characterization of devices and eventually, for biosensing experiments. The patterning of the wafer begins with the application of a resist layer on the wafer. Custom designed micro fluidic channel masks, designed

using commercially available software called DW-2000, are loaded into the mask aligner and the wafer is exposed to UV where the time of exposure is varied depending on the CYTOP thickness and UV lamp intensity.

After the channels are properly patterned on the wafer following careful mask alignment and lithography, the top cladding has to be removed to expose bare gold to sensing fluids on selected arms of the devices. It is these selectively etched openings that are termed micro-fluidic channels. The wafer is exposed to UV plasma where the time of exposure is varied depending on CYTOP thickness and the UV lamp intensity. Once, the channels have been etched, the channel level fabrication process is concluded leaving the devices ready for optical characterization.

The details of the fabrication process are thoroughly discussed in [11], [33] where each step involved in both device and channel level fabrication, is explained in detail. A summary of the process is outlined in the following table.

Step	Description	Details
Device Level		
1	Bottom Cladding of CYTOP on Si substrate wafers	Cladded through the process of spin coating
2	Lithography of stripe devices	Bi-layer lithography used for proper realization of gold devices
3	Gold deposition and resist strip	E-beam metal deposition and wet solvent strip
Channel level		
4	Top cladding of CYTOP on stripe devices	Embeds devices in CYTOP through spin-coating
5	Lithography of microfluidic channels on CYTOP claddings	Aligned to device level lithography for proper placement of channels
6	Patterned etch of stripe devices	Top CYTOP claddings are dry etched with plasma
Device Characterization		
7	Optical characterization	Testing attenuation and insertion losses

Table 1: Summary of the wafer fabrication process. Adapted from [33].

As mentioned earlier, two sets of wafers obtained from two different batches were characterized for the scope of this thesis. Each belonged to a different student with the first batch belonging to the author of [33] and the second belonging to the author of [11]. Table 1 entails the preliminary process followed by both authors [11]. documents extension of work carried out previously in [33] with slight modifications made to the process (an in depth review of which can be found in [33]) in an effort to: a) improve the feature definition on the waveguides b) remove surface roughness of the waveguides and eliminating metal aberrations and c) reducing waveguide deformation. This was primarily achieved by substituting the materials used in bi-layer lithography process, improvising the gold deposition process and reducing solvent use in the upper cladding by increasing bake temperatures, respectively.

3. Interrogation Setup:

3.1 Basic Setup:

A great part of this thesis is dedicated to the characterization and interrogation of numerous waveguide structures designed for the purpose of biosensing. Aside from their geometrical layout (straight waveguides and single or multi-output MZIs), the waveguides generally fell in two categories. Either the devices were left embedded in CYTOP, or the CYTOP layer was etched off the waveguides, leaving their surfaces exposed. In order for a mode to remain bound in the etched waveguides, it was essential to fill the etched cavities with an index matching solution. An array of these structures is illustrated in figure 13 which follows.

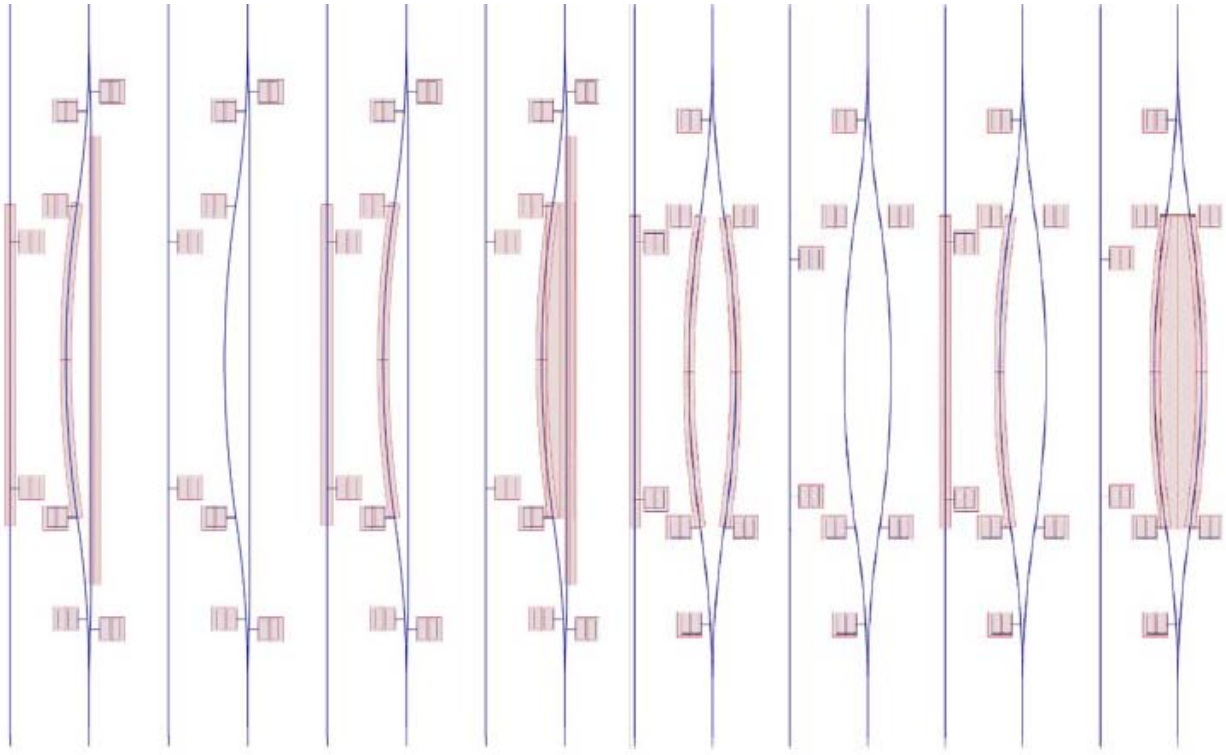

Figure 13: An array of Au waveguides found on a single DIE showcasing a variety of waveguide geometries and etch characteristics. Adapted from [33].

To successfully interrogate these devices by optical means, a setup had to be designed (a task handed over to an independent contractor) capable of fulfilling a number of key requirements. Over the span of the study, a number of changes had to be made to the interrogation setup in order to fulfill the requirements of the project, however some of the features remained unchanged over the period of the study. These features are discussed in this section.

The die consisting of an array of the devices presented earlier in figure 13, is required to be secured firmly in place on a level surface to ensure optimal coupling with a polarization maintaining fiber. The probing fiber itself needs to be secured in a fiber chuck in a manner such that only a short length of the fiber is utilized for coupling with the device. The length of the probing fiber is kept short as a longer cable may be susceptible to air drafts and thus may cause signal variability, which poses a problem during biosensing experiments. Any signal variability induced by noise in the system can make it difficult to spot binding events where analyte binds to antibodies. A collimating lens is required to obtain the mode output from a device under test (DUT) and to ensure signal stability; the lens needs to be mounted securely as part of the setup. The mode output has to be isolated from the radiation which often surrounds it due to device fabrication defects leading to reduced coupling efficiency. Hence a circular aperture is inserted in the beam path which can be opened or closed around the mode output. To monitor the DUT output via an infrared camera and capture the power level simultaneously, a 50/50 beam splitter is introduced, oriented at a 45 degree angle in the optical path to split the signal evenly towards the camera and the photo detector. To ensure that the only component captured by the photo detector is TM polarized, a polarizer is affixed in front of the photo detector and its orientation is adjusted until maximum power output is obtained.

The above mentioned requirements were featured in almost all variations of the setup. Additional measures had to be implemented when characterizing and interrogating devices with etched channels. Circulation of fluids through the system becomes an integral requirement of the bio-sensing apparatus in this case. Therefore, a way to integrate micro fluidic tubing which brought the liquids in and out of the system effectively without any leaks, also had to be considered. In the segments which follow, variations in the interrogation setup employed for testing numerous devices over the span of the study are discussed in detail.

3.2 Setup Design:

3.2.1: Setup Design 1:

Keeping all of the previously discussed requirements in mind, a first interrogation setup was envisioned in-house and handed over to the external contractor for fabrication. The first variation of the interrogation setup consisted of four multi-axis positioners in total. Two of them were five axis positioners with x, y, z, roll and yaw. One with a horizontal and vertical axis only and the last one with vertical axis roll and yaw.

The five axis positioners were used to mount the input probing fiber and a chuck carrying both an output fiber as well as a 25X magnification lens mounted on a sliding chuck allowing switching between viewing the mode and measuring the power output from it. The fibers used were both polarization maintaining fibers with a 7 micron diameter core. The schematics as well as the actual setup is illustrated in Figure 14 a and b which follow.

a)

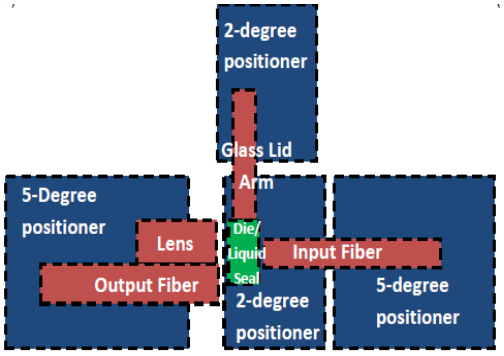

b)

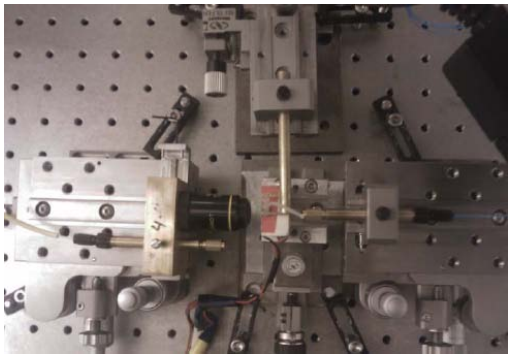

Figure 14: (a) and (b) Schematics and photo of the optical characterization setup (top view). Adapted from [33].

The DUT was mounted on a two axis positioner that allowed adjustments in the X and Z directions. To visually ensure proper alignment of the fibers with the device facets, a microscope was fixed atop the positioner carrying the DUT. A glass lid was attached to a brass arm which was mounted on the remaining multiaxis positioner. This allowed careful lowering of the glass lid on top of the DUT to encapsulate the index matching solution within the etched cavities of the DUT. Two holes were drilled on top of the glass lid. Rubber tubes were attached to the holes which allowed pumping of the solution, in and out of the assembly (see figure 15 b).

A persistent issue was to ensure that the index matching solution could freely circulate in and out of the DUT arrangement without any leaks. This was done by introducing a thin latex 'spacer' with a rectangular hole cut out in the center (see figure 15 a). This spacer layer was carefully introduced between the glass lid and the DUT such that the optical facets were left unharmed. The glass lid was then placed on top of the spacer layer and secured in place with the brass arm designed to gently press the glass lid down.

a) 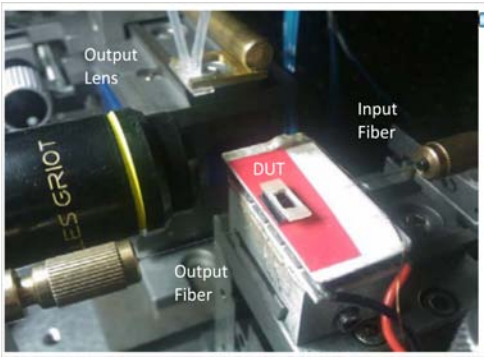

b) 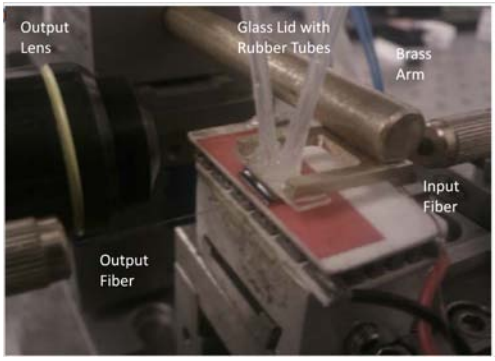

Figure 15: (a) Sample DUT with latex seal on top to prevent leakage of index matching solution. (b) glass lid with rubber tubes pressed upon the seal to encapsulate and circulate solution. Adapted from [33].

The entire assembly formed a flow cell over the device. The alignment of the spacer layer was a key issue as any misalignments would cause the latex to protrude out from under the glass lid and hinder the coupling between the die and the fiber or would cause a leak to spring up, if not pressed properly enough to cause the index matched solution to seep from under the lid. Figure 16 illustrates the schematics of the entire flow cell assembly.

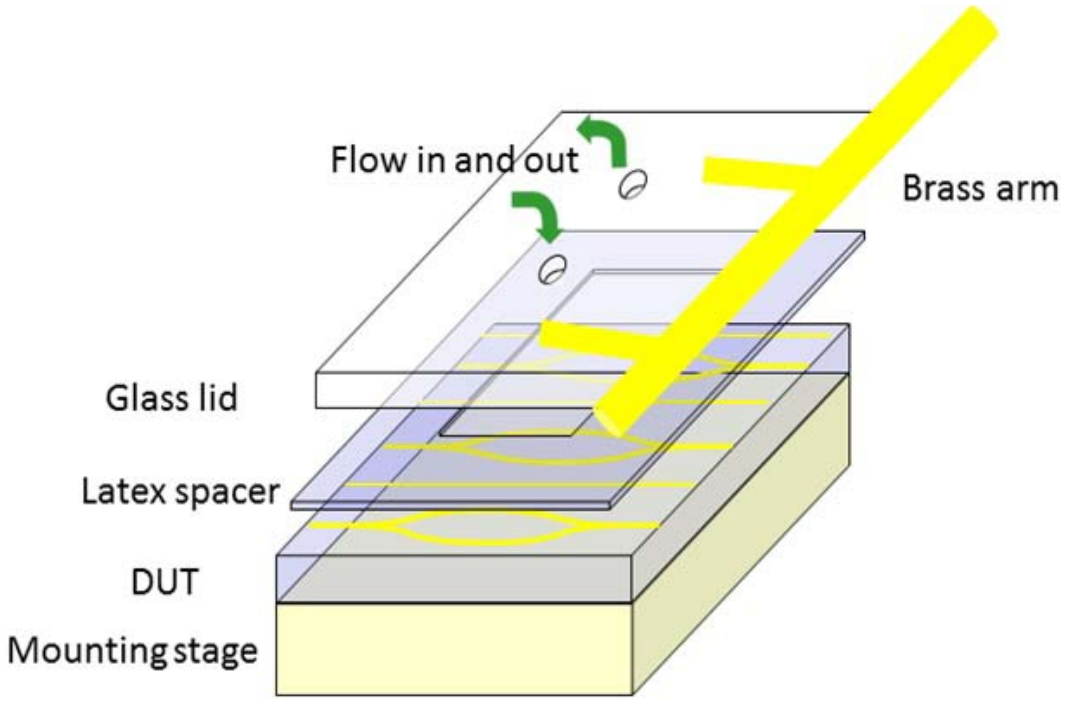

Figure 16: An illustration of the assembly required to encapsulate and circulate the index matching solution through DUT.

This particular setup was equipped with a temperature controlled heat sink which acted as the mounting stage for the DUT and being directly under the die, allowed for fine tuning the refractive index of the index matching solution by varying the temperature of the sink and by extension, the solution itself. The quality of the mode and the power output could be further optimized by tuning the temperature and obtaining ideal index matching conditions.

It is important to note that this particular configuration did not utilize any of the free space optics components which were discussed in the aforementioned introductory basic setup chapter. Since the mode output was only monitored occasionally by switching between the lens and the output fiber, and because the mode power output was obtained by directly coupling the output

fiber (connected to a power meter) to the output facet of the device, there was no need for additional peripherals like the aperture, beam splitter and polarizer etc. An infrared camera with a monitor, were the only additional components, other than the base interrogation platform described in this section for this setup configuration.

3.2.2 Setup Design 2:

In a bid to simplify the setup as well as to reduce the vibration and improve the stability associated with having a large number of moving parts in the interrogation platform, two of the multi-axis positioners were eliminated from the configuration. The two positioners that were retained were the five axis positioners to allow maximum maneuverability. Further modifications were made to the setup as well. The input fiber was mounted on one of the remaining positioners. A custom designed jig (more on the jig design in following sections) was used to carry the DUT and was devised such that it could fit on the rails of the second multi-axis positioner. A 25X magnification lens, used to capture and collimate the beam output, was fixed upon a custom lens mount which was the fixed over the edge of the positioner carrying the DUT. For the interrogation of fully cladded waveguides, the input fiber is aligned such that the input facet of the DUT, sitting snug within the etched groove of the base of the jig, is butt-coupled with the fiber. The output is captured via the collimating lens from where it passes through the aperture, polarizer and beam splitter and on towards the photo detector and the infrared camera simultaneously. Figure 17 a illustrates the schematics of the setup and the equipment layout. Figure 17 b depicts the interrogation platform where the DUT is the centerpiece and is flanked by the probing fiber on one end a capturing lens on the other.

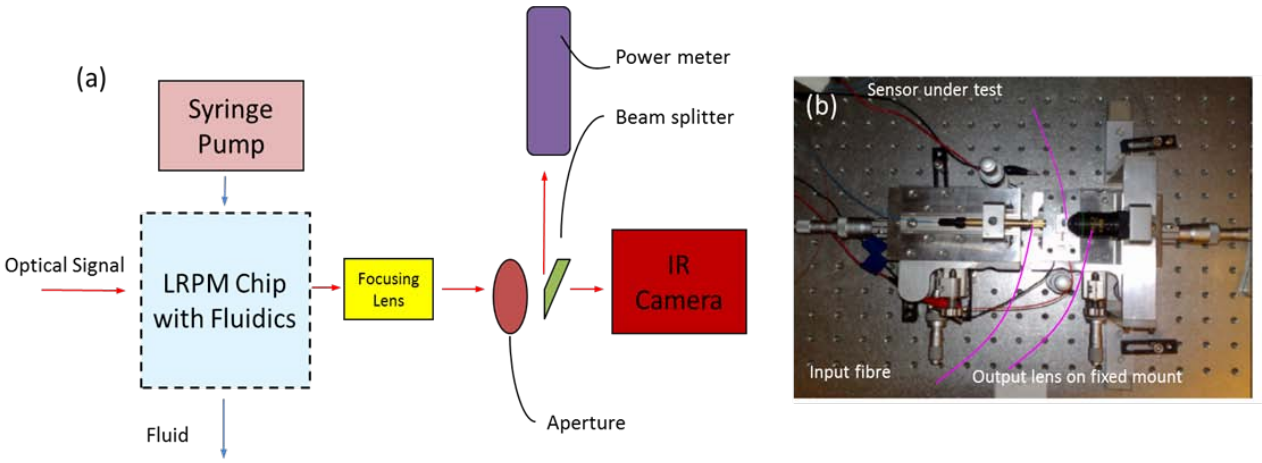

Figure 17: (a) Schematics and layout of the full interrogation setup including the device and surrounding peripherals. (b) Top view of the sensor mounted on the interrogation platform.

3.2.3. Setup Design 3:

The third variation of the setup comprised mainly hardware upgrades in order to enhance the setup stability even further. This was achieved by procuring advanced piezo controlled multi-axis positioners (from Thorlabs) and using them to replace the older five-axis multi-axis positioners (from Newport). One change however was that instead of having 5-axis each on the two new positioners (as was the case for the old one), the positioner selected for mounting the probing fiber, was equipped with and additional sixth axis (x, y, z, pitch, roll and yaw). The second piezo positioner however had a reduced number of axis compared to its predecessor (only x, y and z). As was the case in the previous setup design, the device was mounted on a custom built jig designed to fit the rails of the new positioners. The output collimating lens was affixed once again on a custom brace which in turn was installed over the micro positioner carrying the DUT encapsulated in the test jig. Figure 18 illustrates setup with the said piezo axis positioners along with the accompanying peripherals including the aperture, beam splitter, polarizer, photo detector, IR camera with attenuation wheel and an optical microscope. Though the positioners possessed the capability of

automated control via piezo electric controllers, for the scope of this project, the stages were aligned manually.

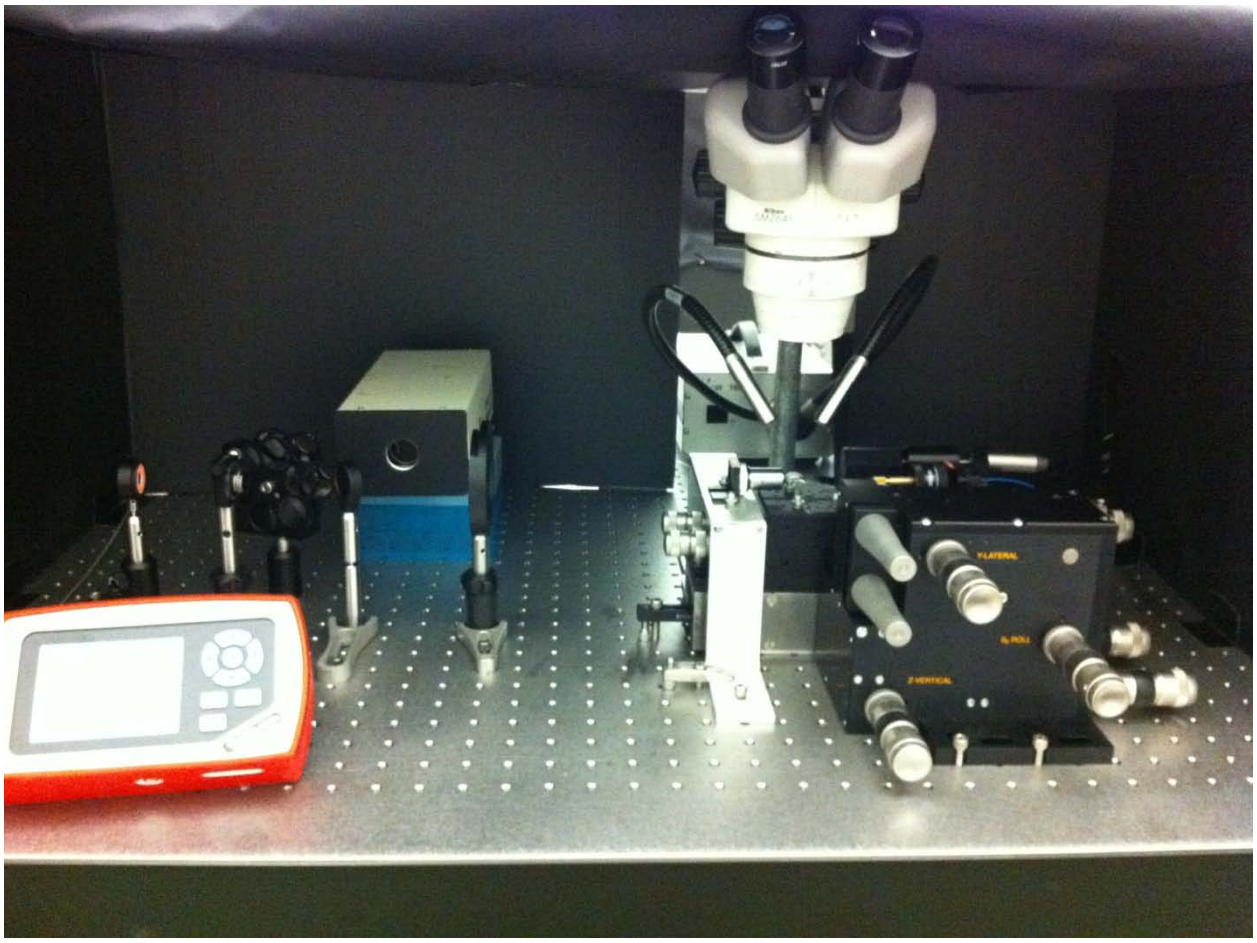

Figure 18: Setup illustration with upgraded multi axis positioners forming the interrogation platform.

3.3. DUT Mounting Jig:

For interrogating devices which are completely or partially etched (with channels or etched segments), a number of approaches were employed over the span of the project. These will be discussed later in sections describing the design of the jig. The key requirement is to ensure encapsulation and proper circulation of the index matching fluid in and out of the device. In all cases, the fluid which is circulated is delivered through the micro-fluidic tubes connected to syringes containing the index matching solutions. The flow of the solutions can be controlled by mounting the syringes on syringe pumps which can be configured to deliver a set volume of solution at a user defined rate.

3.3.1 Jig Design 1:

In the previous section labeled setup design 1, we looked at the initial approach employed to circulate the index matching fluid into and out of the etched channels on the DUT. This required introducing a thin latex spacer over the DUT with a gap carved in the middle to allow the fluid to seep through and into the channels. The spacer layer was held down by a glass sleeve with holes for mounting tubes to bring the liquid in and out. All the components sandwiched together with a brass arm which pressed down on the parts to keep them from moving (see figure 16). This assembly, though functional, was extremely difficult to work with. The alignment of all components had to be extremely precise with very little margin for error. The smallest of misalignments would result in leaks springing up in the assembly or worse, damage to the facets on the DUT rendering the DIE ineffective for further investigation.

In order to make the interrogation of devices easier, first of many jigs were designed in order to allow entry of the fluid into the device channels without going through a tedious and time consuming assembly process (see figure.16).

This was accomplished by fashioning a base with a ridge carved out in the bottom to allow it to sit on and move across the rails of the multi axis positioner. This enabled the distance between the DUT and the optical fiber as well as the collimating lens, to be adjusted as per the requirement of the experiment giving the setup more flexibility. Another ridge was carved on the top of the jig just wide enough to allow the DUT to sit snugly at the bottom (often secured by a double sided tape for extra assurance against movement) flanked by two higher walls that protruded on either side of the ridge to ensure that it remained in place. These walls were also necessary to allow placement of mylar sheets with a known refractive index, over the top and across the back of the jig to provide proper concealment of the index matching solution. The mylar sheets were held in place using clear epoxy. The front of the enclosure was however left untouched to allow the placement of the DUT within the jig, where it could simply be slid in and out of the groove etched within, to keep it securely in place. Two holes were drilled on either side of the flanking walls, all the way through leading into the enclosure itself. Two small tubes fashioned out of aluminum were permanently affixed into these holes which brought the solutions into and out of the enclosure. These tubes could be extended further by attaching external rubber tubing over the aluminum tubes which could in turn be connected to a syringe to facilitate the delivery of various solutions pumped. Figure 19 and 20 depict the front and the top view of the jig respectively.

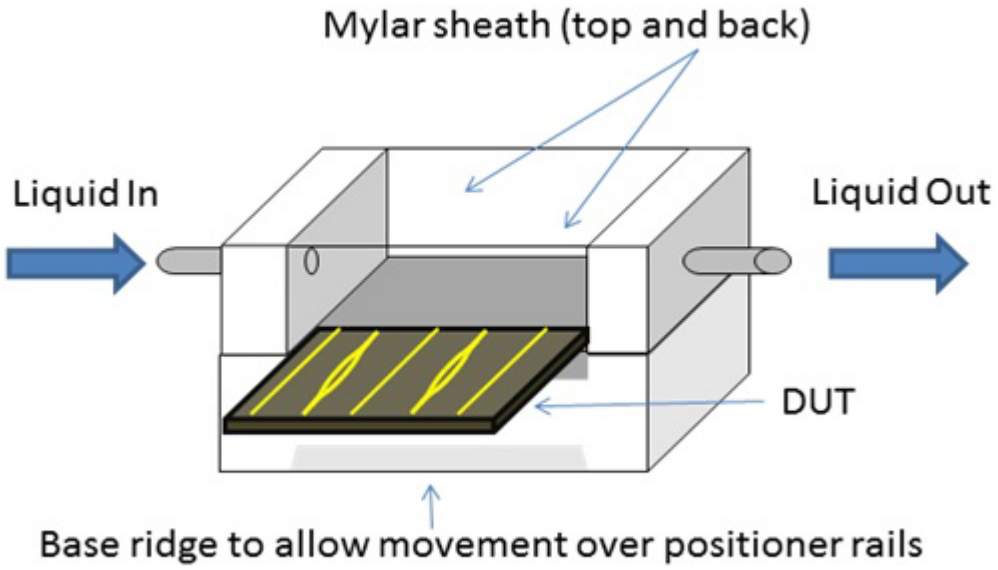

Figure 19: Schematics entailing side view of jig 1 indicating point of entry for the DUT as well as the liquid going in and out of the jig.

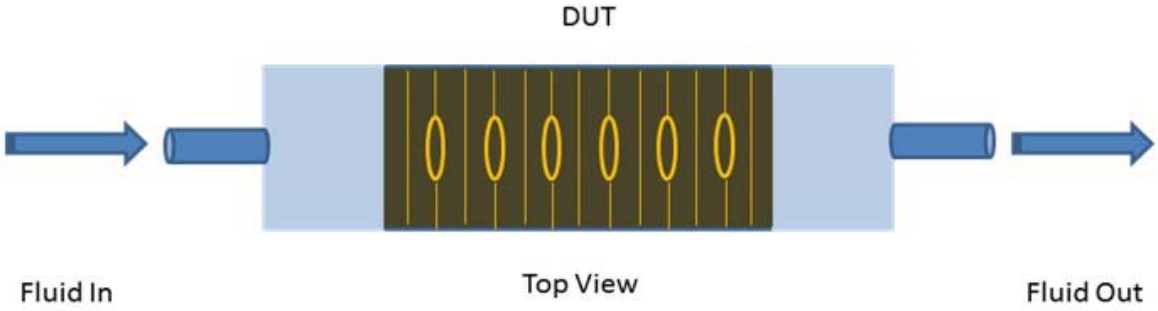

Figure 20. Schematics entailing top view of jig 1 illustrating a device mounted under mylar sheet and the fluid entry and exit points.

This configuration, though practical, had one major drawback associated with it. This was the gaping hole left at the front of the enclosure to allow the insertion of DUT. For the most part, the liquid entering the enclosure remained within the confines as a result of capillary forces.

However, one had to be careful when delivering the solution into the enclosure, not to inject excessive liquid. The increased pressure would overwhelm the capillary forces holding the solution within and would result in the spilling of the solution from the open gap in front of the enclosure. Another problem was that the repeated use of varying index matching solution would lead to the interior of the mylar sheath getting dirty. Due to the small size of the enclosed space, it was difficult to reach within the enclosure to clean the mylar and a dirty sheath resulted in additional attenuation of the output beam. This could only be resolved by frequent replacement of the mylar which was a time consuming process.

3.3.2. Jig Design 2:

The leaks as well as the constant need to replace the mylar had to be eliminated from the setup and therefore required redesigning of the jig. Once again, the requirements that had to be kept in mind were to ensure that the setup remained free of leakages and allowed the DUT to be mounted securely throughout the experimental process. The ideal means for achieving this feat would be to design schematics such that the etched cavities on the DUT were confined within an enclosure capable of encapsulating and circulating the solution within its confines, yet the edges of the DUT were still exposed, allowing butt coupling of the fiber with the input facets.

Over the course of the study, numerous DIE's with a variety of etch configurations were used. It was hence optimal to find a configuration that would allow seamless integration of all these DIE's (straight etched channels over single waveguide, a circular etch encompassing a number of straight waveguides on a single DIE, a 'snake' etch with a single etched cavity snaking horizontally along the length of the DIE forming etched channels of varying lengths over a number of waveguides, etc) within a single newly designed jig.

After careful considerations and planning, a new jig was devised. Once more, a custom base was designed such that it allowed for situating the DUT on top (where its positioned atop an additional platform) and the bottom of the jig could be fitted on the rails of the multi-axis positioner facilitating the positioning of the Die at an ideal distance from both the probing fiber and the focusing lens (see figure 22 b), as it sits between the two. A slip cover is fashioned out of see through Plexi-glass, the dimensions of which are matched to that of the platform wielding the DUT. This would allow for the positioning of the slip cover over the Die once it's affixed within the groove etched on top of the platform. Two holes are screwed on either side of the Die on the platform. Holes are also drilled into the Plexi-glass, the distance between the two as well as the dimensions of the holes are matched to that of the base platform. This enables sandwiching of the DUT between the slip cover and the Die platform. Some of these details are illustrated in Figure 21 which follows:

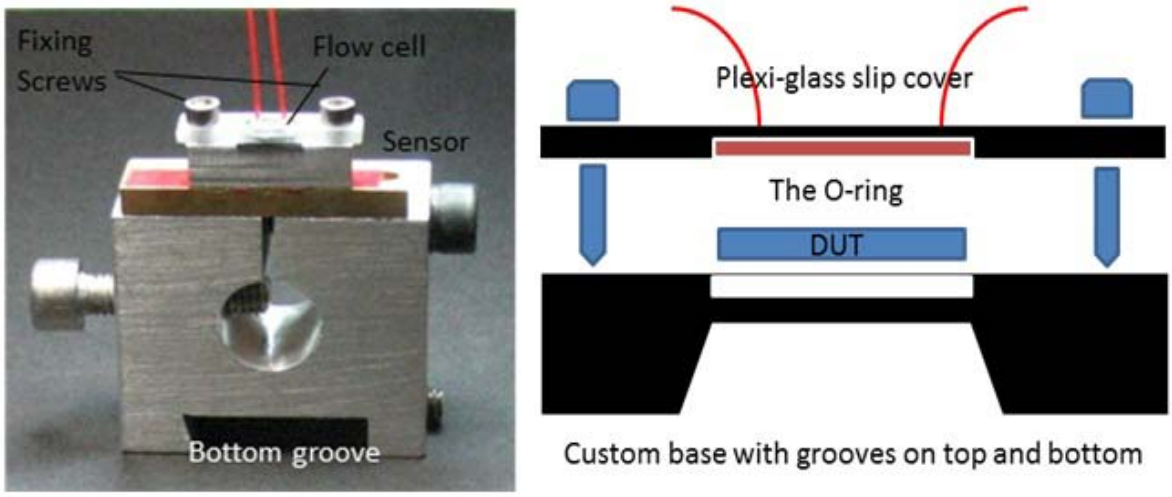

Figure 21: Photo and schematics of jig design 2 illustrating the DUT assembled within the jig along with various components facilitating the device assembly and flow of the solution.

The bottom of the cover slip has a shallow groove etched on its surface which allows for a rubber o-ring to sit within the channel. The o-ring is permanently attached to the channel by using an epoxy which is allowed to cure (after the o-ring is affixed) for half an hour. The attachment of the o-ring to the slip cover using the epoxy requires extreme care and finesse using as little of the epoxy as possible since excessive epoxy would shed a residue into the bio-sensing solutions, potentially contaminating the samples and tampering the refractive indices. The rubber o-ring extrudes out slightly from the groove forming a flow cell when the cover slip is screwed on top of the platform carrying the DUT. Two smaller holes are drilled near the center of the cover slip within the confines of the o-ring. This allows two micro fluidic tubes carrying the sensing solutions into and out of the jig, to be attached on top of the slip cover (see figure 22 a).

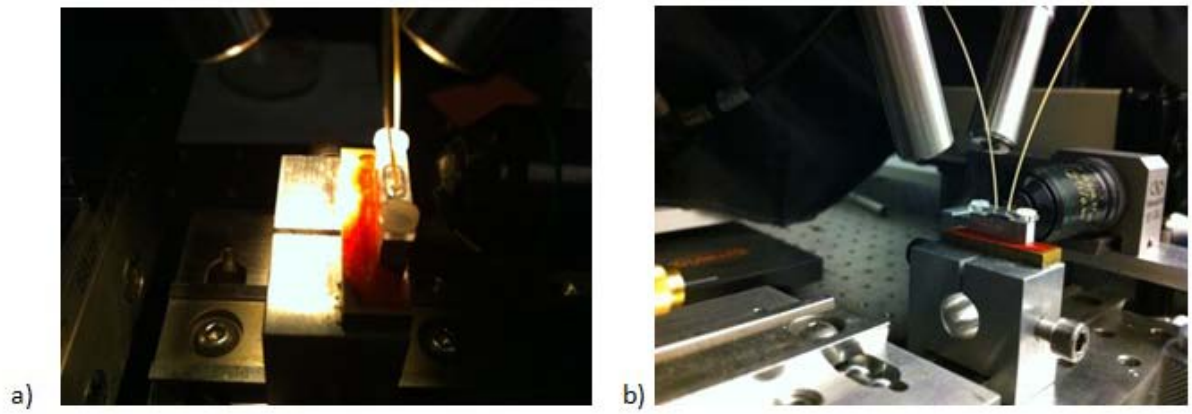

Figure 22: (a) DUT assembled within the jig enclosure with entry and exit fluidic tubes protruding (b) DUT prepared and ready for optical interrogation via probing optical fibre and an output lens combination.

The attachment of tubing to the holes is also a task which requires great care and poise since the end of the tube going into the hole must be level with the bottom of the hole. Care must be taken when fixing the tube such that it doesn't protrude out from the bottom of the hole.

Otherwise the stiff end of the tube may come in contact with the DUT and scratch the CYTOP surface. On the other hand, if the tube leaves a gap between itself and the bottom of the hole, the air trapped within this gap can be driven forward when the solution is pumped through, resulting in the formation of an air bubble within the confines of this flow cell. This air bubble prevents the solution from entering the etched channels on the DUT surface preventing the formation of the fluidic cladding layer over the etched channels and hence affects the sustained propagation of a mode.

Formation of air bubbles is undesirable and it takes tedious care when assembling the DUT within the test jig to prevent it from occurring. The procedure requires carefully aligned placement of the die within the groove etched on the base of the jig. A small piece of double sided tape can aid in keeping the die firmly in place. A small droplet of index matched solution is placed on top of the die. A syringe containing the index matched solution is attached to the microfluidic tube which in turn is connected to the cover slip. The plunger on the syringe is carefully depressed until a small droplet is released underneath the cover slip and forms a film of solution within the o-ring glued to the underside of the cover slip. The cover slip is then carefully pressed down upon the metal base carrying the DUT and is screwed down quickly before most of the solution can escape leaving room for air to form bubbles underneath.

Another precaution that is employed to prevent formation of bubbles within the fluidic cell is by discouraging air from getting trapped under the droplet suspended over the DUT. The use of the fluoropolymer CYTOP in the fabrication of devices causes the DIE surface to become hydrophobic. This results in air getting trapped under the solution droplet suspended over the DUT, but not quite laying flat on the surface due to its hydrophobic nature. Hence before mounting the device on to the jig, it is treated with carboxyl in order to make its surface relatively hydrophilic. The

procedure consists of rinsing the devices in an acetone bath for 10 minutes followed by a bath in isopropyl alcohol (IPA) for an equally long duration. IPA is more commonly known as rubbing alcohol with the molecular formula of C_3H_8O. It is known to dissolve many materials including many oils and natural resins [34]. This property is used to help the devices shed the residual photo resist film left on their surface after the fabrication is complete. Next the devices are placed in a Petri-dish and left uncovered in a UV-ozone chamber for half an hour. After exposure the dies are removed and immediately immersed in carboxyl (or 16-mercaptohexadecanoic acid; used a solution of 2 mM in IPA) where they are left for an hour. After an hour, the dies are removed from carboxyl and blow dried with nitrogen. Finally the dies are washed with IPA and are then ready to use, possessing relatively hydrophilic gold surfaces. The application of carboxyl terminated thiol interacts only with the Au waveguides leaving the CYTOP surface intact and hydrophobic to facilitate the access of sensing fluids onto the waveguides.

3.3.3. Jig Design 3:

The latest generation of devices employs side channels for fluid delivery, see figure 23, where the yellow regions represent etched areas where the waveguides are exposed to the sensing fluid. Single sensing arms are exposed to fluid delivery in figure 23 a, while 23 b demonstrates a device where both sensing and reference arm have been etched.

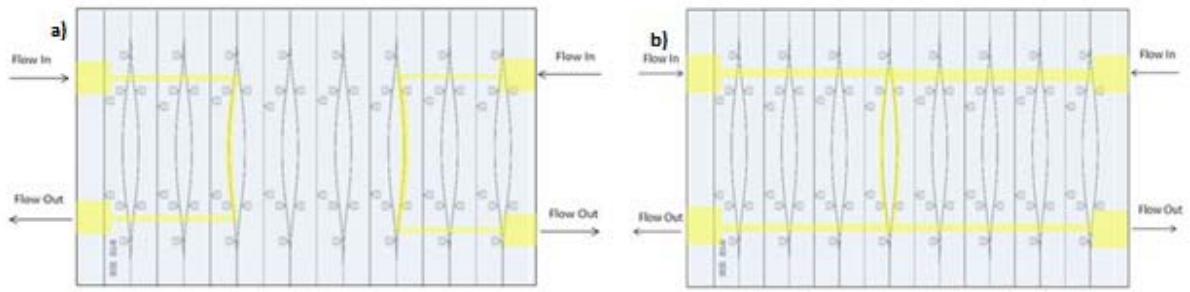

Figure 23: (a) Single-Arm MZI – individual microfluidic channels are provided for only a sensing arm and (b) Double-Arm MZI – microfluidic channels are etched for both sensing and reference arms. Adapted from [12]

This variation for fluid delivery is employed for longitudinal delivery and flow of the sensing fluid as opposed to the fluid delivery from the top of the device from where it spread into the channels. This variation consumes less fluid sample volume and should lead to a lower limit of detection due to improved control of the flow conditions. A new jig had to be designed in order to characterize these devices. The new jig had to be configured such that it enabled delivery of the fluid to the device from either side through the channels marked 'Flow in' on the figure 23. Expelled liquid coming out of the 'Flow out' channels also had to be taken care of such that it exited the jig after circulating through the DUT. As always, the jig design had to incorporate features that allowed for situating the DUT snugly within an enclosure which was capable of encapsulating the sensing fluid within the confines of the device channels and prevented leaks and over spills from the sides (see figure 24).

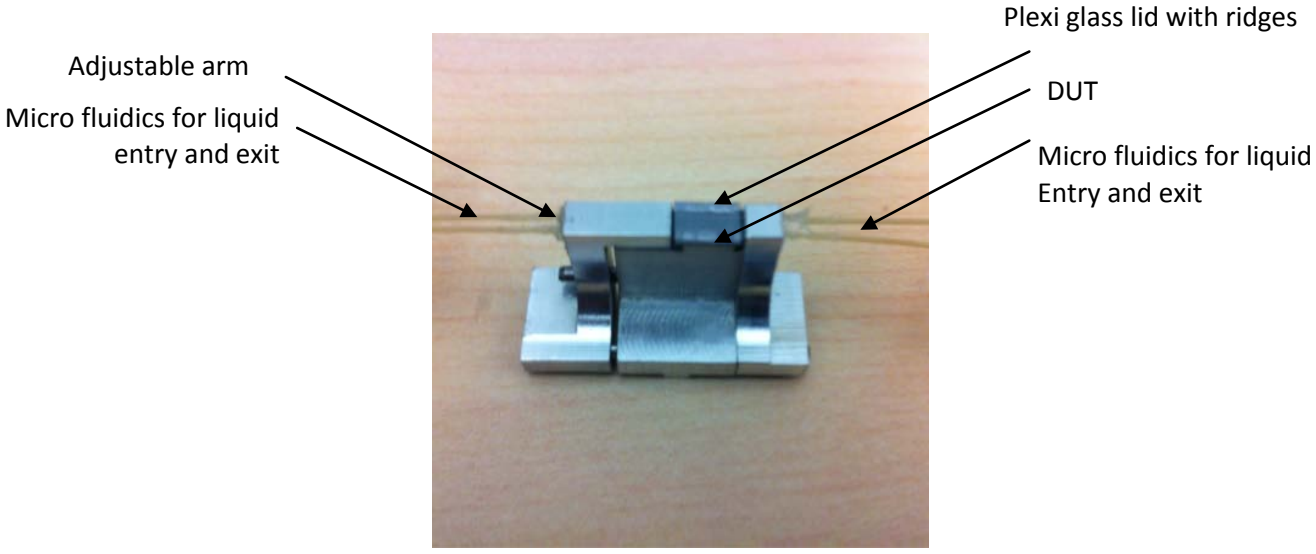

Figure 24: Latest jig developed for device interrogation with side channel access for fluid delivery and clear plexi glass lid with silicone ridges designed to discourage fluids from leaking.

4. Setup Stability:

One of the most important factors associated with the acquisition of optical signal from a mode output excited in a waveguide, is the stability of the setup. An unstable system can cause unwanted noise and drift in the measurements. A number of factors can affect the stability of the system. For instance, the air flow in the room can cause the optical fiber to sway about causing the mode output to fluctuate. Similarly, the mechanical drift in the multi axis positioners can result in the fiber, as well as the device, to move from its original location. This drift in turn can adversely affect the results. The lighting in the room can also be picked up by the photo detector which has a sensor, equipped to handle a wide range of wavelengths. This is another reason that can compromise the results acquired.

Keeping all of the above factors in mind, precautionary measures had to be taken to ensure that the interrogation setup was free of the aforementioned flaws. To isolate the system from the air flow circulating it the room, as well as to minimize the intrusion of stray light from disturbing the setup, an enclosure is fashioned out of stiff cardboard such that it surrounds the interrogation setup completely. Small holes are carved in appropriate places to let connective cables for devices such as the infrared camera and the photo detector come through. A slightly larger hole had to be cut in order to allow the extending arm of the microscope which is positioned above the micro positioners where the DUT is held. Another large hole is carved out to allow ‘goose necks’ to enter and be fixed over the setup in order to illuminate the device going through an inspection under the microscope. The cardboard enclosure surrounds the setup from the back and the sides. The front of the enclosure is fashioned out of thick black fabric so that one can easily access the setup in order to mount, dismount, align and inspect the DUT by simply moving the fabric in and out of the way.

4.1 Stability Testing:

The stability of the setup was optimised prior to conducting any experiments in order to ensure that there were no vibrations or fluctuations associated with the interrogation mechanism which may affect the measurements. This enabled acquisition of a baseline against which the experimental results were compared.

The variation in power is monitored by writing a program in LabVIEW which plots the power values acquired from the photo-detector, against time. The optical fiber is aligned such that the best possible power output is measured by the photo-detector. Alternatively, a test DIE can also be inserted in the setup where a mode is excited in a straight cladded waveguide and the mode output is captured by the photo-detector, at which point the enclosure around the setup is sealed completely to prevent stray light from entering the unit. The output power is then recorded over a span of 15 to 20 minutes. The variation of setup can then be measured by differentiating between the maximum power output recorded and the minimum power. The chart in figure 25 illustrates the mode stability output obtained from a straight cladded waveguide tested on setup design 1, 2 and 3 respectively. The mode power output was recorded for approximately 20 minutes.

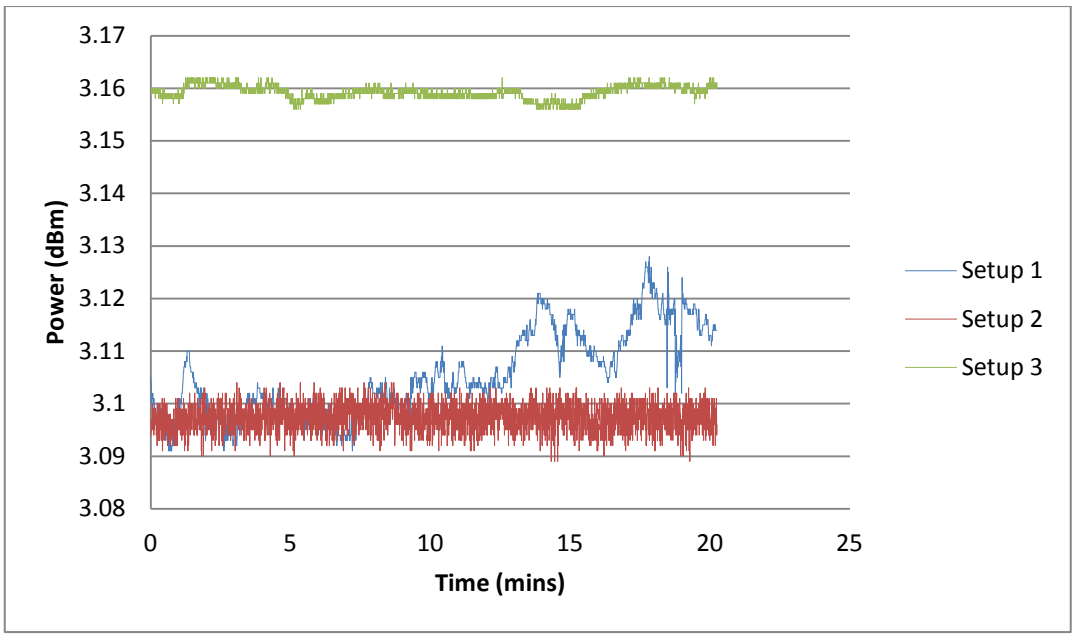

Figure 25. The stability curve for the three setup variations described. The stability is plotted as a function of output from a straight cladded waveguide over a period of time.

The chart in figure 25 is an illustration of the stability variation between setup design 1 and setup design 2 where setup design 2 holds a clear edge over setup design 1. As apparent from the stability curve, setup design 1 remains fairly stable over the span of approximately ten minutes after which, there is considerable variability in the signal. There is also significant drift in the signal after ten minutes. The stability curve obtained from setup design 2 in contrast, is fairly stable as it exhibits much lower noise and signal drift. This can be attributed to the simpler setup design with the least amount of moving peripherals possible. Setup design 3 trumps the previous two layouts by offering a considerably higher stability over the entire span of the experiment. Introduction of more advanced hardware (piezo positioners), affords setup 3, much higher stability in comparison to its predecessors. Parameters such as maximum and minimum powers etc are presented in table 2 which follows:

	Setup 1	Setup 2	Setup 3
Maximum	3.128	3.104	3.162
Minimum	3.091	3.089	3.156
Average	3.105	3.097	3.159
Standard Deviation	0.008108	0.002641	0.001339
Maximum-Minimum	0.037	0.015	0.006

Table 2: Parameters such as min/max/average power output of a straight cladded waveguide recorded over a span of 20 minutes to evaluate setup stability.

5. Bulk Sensing Measurements:

5.1. Overview:

As discussed in an earlier chapter, device structures of various types including straight waveguides and Mach-Zehnder interferometers are incorporated in the platform in order to allow flexibility for sensing a wide range of analytes. Selective etching allows for configurations where a single arm on a Mach-Zehnder interferometer is etched while the other was left cladded allowing it to act as a reference arm (see figure 26).

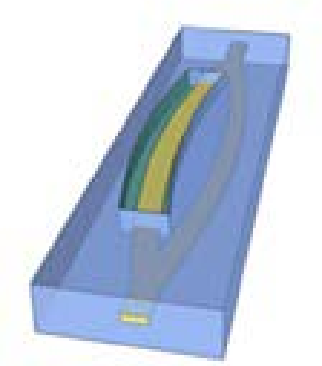

Figure 26: A Mach-Zehnder Interferometer, partially embedded in CYTOP polymer with a fluidic channel etched over the sensing arm of the device.

The etched arm of the interferometer was filled with the bio-sensing solution carrying analytes where a key requirement for the LRSPP platform to function in accordance with specifications is to meet the condition where the refractive index of the sensing solution is matched

to that of the substrate. Refractive index of water is determined to be 1.3330[29] a value which is relatively close to the refractive indices of most biologicaly compatible solutions.

Most polymers have refractive indices which are considerably higher than that of water. In order to ensure that the refractive indices of the layer beneath gold waveguides and the biological solution is matched, a polymer with a refractive index close to that of water had to be chosen. CYTOP, which is a flouropolymer, with a refractive index of 1.3348 at 1300 nm wavelength [34], was selected for this purpose. The commonly used biological buffer solution PBS (Phosphate Buffer Saline) has a refractive index of 1.325. To offset the mismatch in the indices value, the PBS solution is mixed with varying levels of glycerol.

A number of solutions with varying refractive indices were prepared by changing the concentration of glycerol. By adding glycerol to the stock buffer solution, the refractive index of the solution is progressively increased. Similarly, the refractive index of the solution can be reduced by dilution with water. The refractive index of stock buffer solution as well as the refractive indices of subsequently prepared solutions are measured by a prism-coupler based instrument (Metricon) in order to ensure the validity of the index value.

5.2 Metricon Validation:

The laboratory is equipped with a Metricon model which is a device capable of measuring the thickness of the sample film as well as it's refractive index. The principle of operation of the machine consists of a laser beam striking the base of a high refractive index prism and then reflecting onto a photodetector. A thin film of the solution to be measured is smeared onto a coupling head which is brought into contact with the base of the prism with the help of a pneumatic arm. The prism, along with the sample to be measured, the coupling head and the photodetector,

are mounted on a stage that can be rotated. This allows the angle of incidence of the laser beam, to be varied. As the angle of incidence changes, at certain angles, called mode angles, photons escape from the total internal reflection criterion and enter from the base of the prism into the sample film where they enter into optical propagation modes, causing a drop in the intensity of light striking the photodetector. The change in intensity is plotted as a function of the change in angle of the incident light. This is illustrated in the figure 27 which follows:

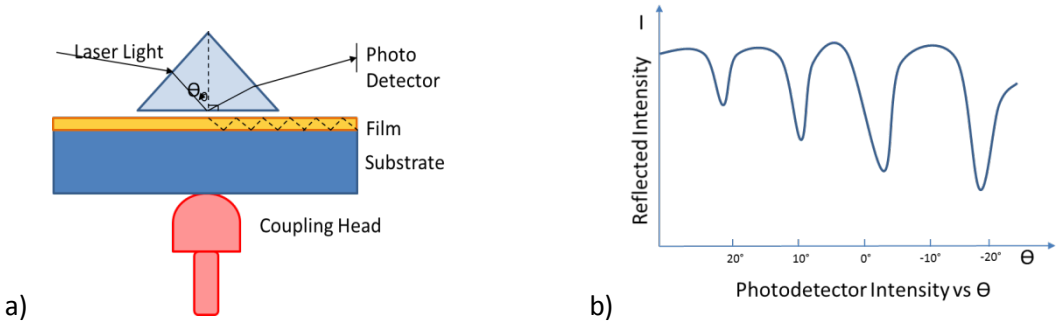

Figure 27 (a). Investigation mechanism inside the Metricon devised to measure refractive index of solutions (b). Change in reflected intensity plotted against a change in the angle of incident light.

For a given sample, the angular location for the modes depends on the thickness of the film as well as the refractive index. Once the two mode angles are determined, the refractive index as well as the film thickness can be calculated by a preprogramed algorithm. This algorithm benefits from the angle of incidence which determines the phase velocity in *x* direction, $v^{(i)} = c/n_p \ Sin\theta$, of the incident wave in the prism (index n_p) and in the gap. A strong coupling of light into the sample film is only possible when a θ is chosen such that $v^{(i)}$ equals the phase velocity v_m of one of the characteristic modes of propagation in the guide (m = 0,1,2...). By determining these synchronous angles θ_m of strongest coupling, characteristic propagation constant of any given sample film, relative to the propagation constant k of free space, can be determined experimentally, where $k = \omega / c$.

Given $N'_m = c / v_m = n_p Sin\theta_m$, we can calculate theoretical values N_m for the relative propagation constants from the known dispersion equation of a planar dielectric waveguide which is stated as follows:

$$N_m = N\,.\,(m, n, W, k, n_0, n_2, \rho). \qquad \text{- (Equation 3)}$$

Where, n_0 and n_2 are refractive indices of the two media adjacent to the film ρ indicates the polarization of the laser beam ($\rho = 0$ for TE polarized light and $\rho = 1$ for TM polarized light). All parameters are known and can be measured separately. The computational problem then boils down to adjusting the two unknown parameters n and W until the resulting theoretical values N_m match as closely as possible to the experimental values $N'_{m.}$ [35].

5.3. Bulk Sensing Measurements:

For bulk sensing measurements, six solutions of varying refractive indices were prepared. The refractive index is adjusted by starting off with PBS solution with the base refractive index of 1.32136 and adding glycerol with a known refractive index of 1.4631, to it. As an example, a table depicting the desired refractive index with the amount of glycerol required added to the base solution to achieve it, is illustrated below:

Desired 'n'	Added Glycerol (g) to 50 mL of PBS solution
1.328	2.93
1.33	3.88
1.332	4.875
1.334	5.906
1.336	6.972

Table 3. The amount of glycerol added to base PBS solution in order to achieve desired refractive index.

The refractive index of each was measured with the help of the Metricon and the values obtained were: 1.324, 1.326, 1.328, 1.330, 1.332 and 1.334 respectively. The solutions were sequentially injected into the setup consisting of the DUT which was aligned such that the input fiber was butt coupled into a straight etched waveguide (a Mach-Zehnder interferometer would work just as well, however a straight waveguide was used for the sake of simplicity) where its position was optimized until a mode output was obtained. Once the plexi-glass slip cover, with an o-ring underneath and micro fluidic tubes attached to the top, is set over the DUT, it forms a flow cell where the series of solutions can be sequentially injected via the tubes, into and circulated in the cell (Refer to figure 20). Once the etched channel over the straight waveguide is filled with the index matching fluid, the power of the mode output obtained is measured and noted against corresponding index matching fluid.

The sequential injection of the series of fluid, into the flow cell is repeated to ensure that the power levels corresponding to a solution with a specific refractive index are reproducible. If this

feat is attainable without having to realign the interrogation setup, then the stability of the sensing platform is also verified along with the refractive indices of the solutions.

The aim is to determine an optimally matched refractive index solution among the range of solutions provided, suitable to carry out bio-sensing experiments. This required inspection of mode outputs obtained from each of the solution used, for intensity of the mode as well as the radiation surrounding it. The ideal mode output consisted of a high intensity mode surrounded by little to no radiation.

At 1310 nm, the refractive index of CYTOP is known to be 1.330. However this may vary slightly after it is deposited on devices. To compensate for this variation, a nominal solution with the refractive index matched to that of CYTOP was prepared along with a few more with refractive indices which increased and decreased in steps of ~0.002 from that of the nominal solution. A solution with the refractive index of 1.324 was used to initiate the experiment to obtain a mode and align the setup. A high quality image of the mode output was obtained using an infrared CCD camera and was saved for later inspection. The solution was then replaced with another with a refractive index of 1.326 and the same process was repeated for all the refractive indices up to the solution with an index of refraction of 1.334. The images were then visually inspected to determine the best output in accordance with the guidelines which were previously discussed. Figure 28 consists of a sequence of mode output images captured under the same imaging conditions discussed above.

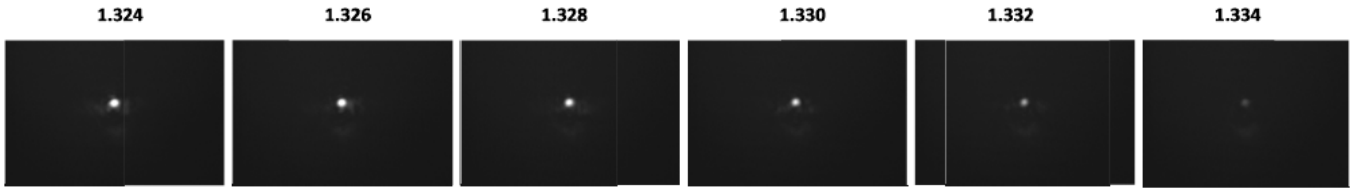

Figure28: Series of mode outputs obtained by testing a single waveguide covered by a series of solutions with varying refractive indices.

After comparing the outputs and judging them against the specified criteria of mode intensity and radiation profile, the refractive index of 1.326 was determined to be the solution which produced a bright and clean mode output with the least amount of surrounding radiation. This solution was subsequently used in carrying out preliminary bio-sensing experiments to detect presence of bacteria on waveguides. Figure 29, is of a chart which depicts the power of the signal over time as solutions of varying refractive indices were sequentially injected in the flow cell. The solutions were repeatedly injected and their response was monitored over a span of approximately an hour and a half. This was done to demonstrate the accuracy of the DUT/Setup combination and its ability to recover the power signal associated with a corresponding refractive index solution.

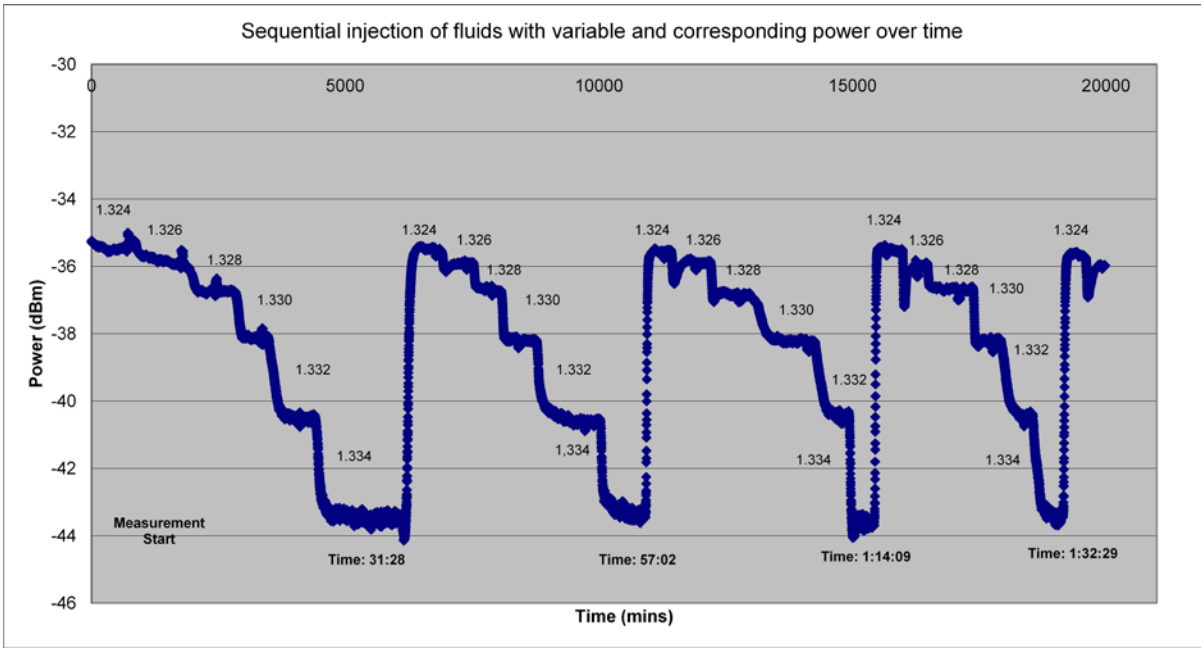

Figure 29: Power of mode output measured over time with sequential injection of index matched fluid with variable refractive indices

The mode outputs illustrated in figure 28 correspond to the steps which are demonstrated in figure 29.

6. Device characterization results

Over the course of the research conducted for the scope of this thesis, a number of wafers that came out from the fabrication lab at Carleton University, prepared by various students, were tested. This chapter will report characterization results acquired by optically interrogating these wafers, fabricated along the course of evolution of the fabrication process related to improvements in surface roughness, waveguide quality, channel variations and other features.

Devices from the wafers are characterized in a bid to obtain a cutback curve which in turn allows extraction of invaluable parameters for gauging the quality of the wafers like the Mode Power Attenuation (MPA) as well as the coupling losses associated with the end facets on either end of the waveguide. The process consists of selecting and measuring the mode output from high quality waveguides with clean end facets. The cleaning process consists of immersing DIEs of interested in an acetone bath for 15 minutes to peel of the residual layer of resist that is left on the wafers at the end of the fabrication process. Next, the DIEs are immersed in an IPA wash for another 10 minutes to rinse off any remaining particulates. Finally the DIEs are dried with a nitrogen jet. The quality of the waveguides is inspected under a microscope to ensure that the DUT are free of abrasions resulting from either fabrication or dicing process. Devices with visible cracks or bends in the waveguide are also rejected.

The process requires that waveguides of three different lengths (3mm, 3.8 and 4.8mm) are selected. This is necessary in order to generate a proper cutback curve. A calibration measurement is obtained first to eliminate from the setup any power losses associated with the fibers and other instruments in the optical path. For setup 1 variation, this was done by aligning the input fiber and the output fiber directly against each other and measuring the input laser power output over time.

For all other setup variations, the calibration measurement was acquired by aligning the optical power output from the input fiber through the collimating lens such that it passed through the instruments in the optical path and reached the photo detector which measured the power output over time.

After the initial calibration, the DUT is placed in the optical path between the interrogation fiber and the output capturing means, be it the output fiber directly or a photo detector via the collimating lens and other miscellaneous peripherals. The captured output consists of an excited LRSPP mode obtained after careful alignment of the TM polarized input fiber to the input facet of the DUT. The IR camera is necessary during the alignment process to observe the mode output as the fiber alignment is varied to ensure maximum possible output with the least amount of radiation associated with substrate/cladding scattering. Once a proper alignment is achieved, the mode output obtained is usually easily distinguished from the surrounding radiation due to its bright profile compared to the scattered light, strong localization, sharp focus and readily extinguishable nature with the smallest of changes in the fiber alignment.

Once a proper alignment with the probing fiber is achieved, the power output associated with the resulting mode can be acquired via the output fiber or from the photo detector aligned with the setup, depending on the setup variation. In the case of acquiring the power output via the output fiber, the measurement is conducted by replacing the microscope objective, used to visually acquire the mode output, with the output fiber once the mode is spotted. From here onwards it's a matter of fine tuning the position of the fiber and monitoring the real time power values on the power meter which the fiber is connected to, until a maximum power value is obtained. In the case of measuring the mode power via the photo detector, the process is simpler. It is a matter of

aligning the device with the input fiber such that the output mode exits through the collimating lens and is projected onto the center of the sensing surface of the photo detector.

The cutback curve is obtained by plotting the insertion loss values against the length of the devices. The insertion loss values are calculated by subtracting the measured output power from the initial fiber input power. The slope and the intercept obtained from linear extrapolation of the curve, gives the values for Mode Power Attenuation (MPA) and the facet coupling losses respectively. Cutback curves obtained from a number of devices belonging to different wafer batches, measured through the course of the study are presented below.

6.1. Un-cladded Waveguides:

The insertion loss of two series of straight waveguides of different length with diced end facets, originating from a single wafer (CT5) [refer to appendix in 33], was measured. The measurements were obtained at a wavelength of 1310 nm. The upper cladding for the etched waveguides consisted of an index matching fluidic layer deposited on top of the DUT. Figure 29 plots the measured insertion losses versus the waveguide length (cutback curves). Each series of results comprises of three straight waveguides of lengths 3.0mm, 3.8mm and 4.8mm. Both series were found to exhibit good linear fits. The measured MPA values for the two series were 7.37 and 7.57 dB/mm respectively. Compared to the theoretical value of 7.2 dB/mm obtained via simulations performed in [34] (for 5µm wide and 35 nm thick gold waveguides embedded in CYTOP), the calculated MPA error for the experimentally obtained values is 2.4% and 5.1% respectively. The inset in figure 30 of the cutback plot demonstrates the mode output obtained.

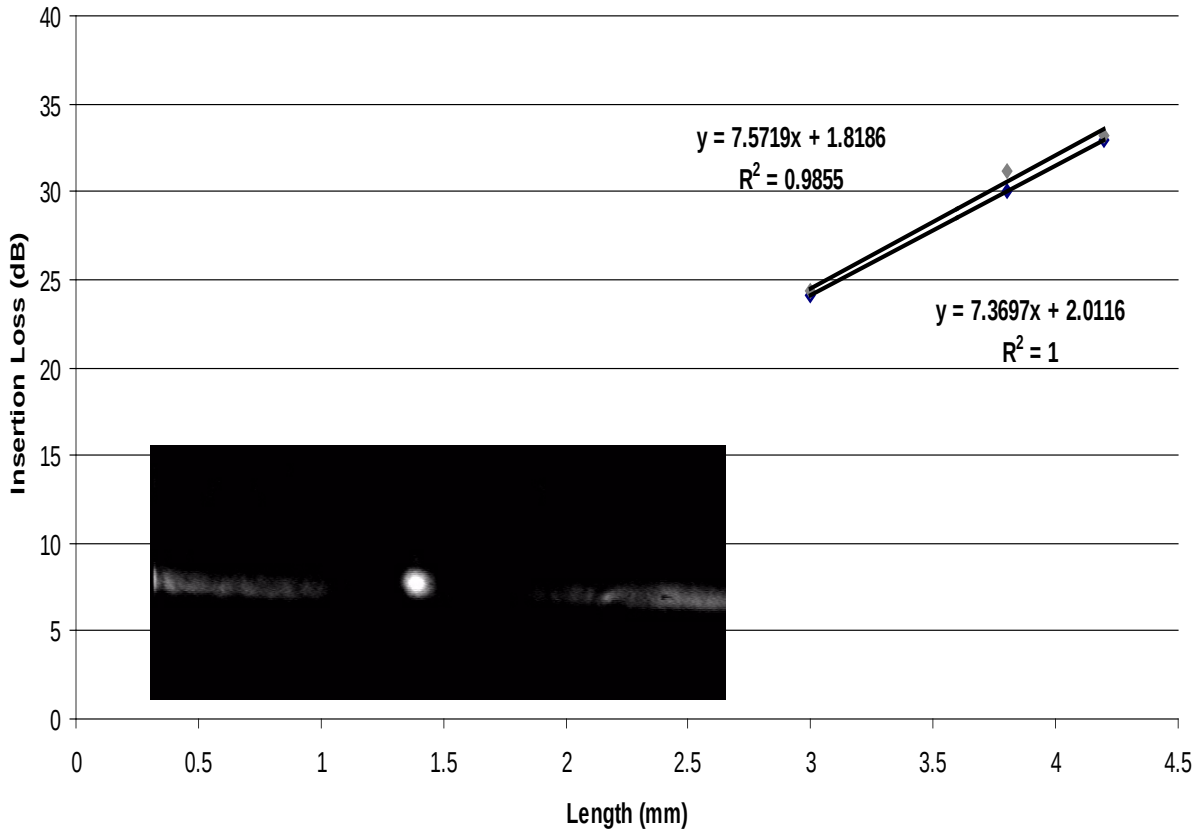

Figure 30: Cutback curve and insertion losses for CT5 wafer.

6.2 Cladded Waveguides:

Insertion losses for straight cladded waveguides of different lengths were extracted from devices retrieved from two different wafers (CWS 19 and CWS 24). Figure 31 depicts the cutback curves along with the inset which shows the mode output of one of the waveguides. The measured average MPA value for the curves was 6.32 dB/mm and the measured average coupling loss per facet was 0.38 dB. These values were compared against the theoretical values of 7.8 dB/mm and 0.89 dB respectively.

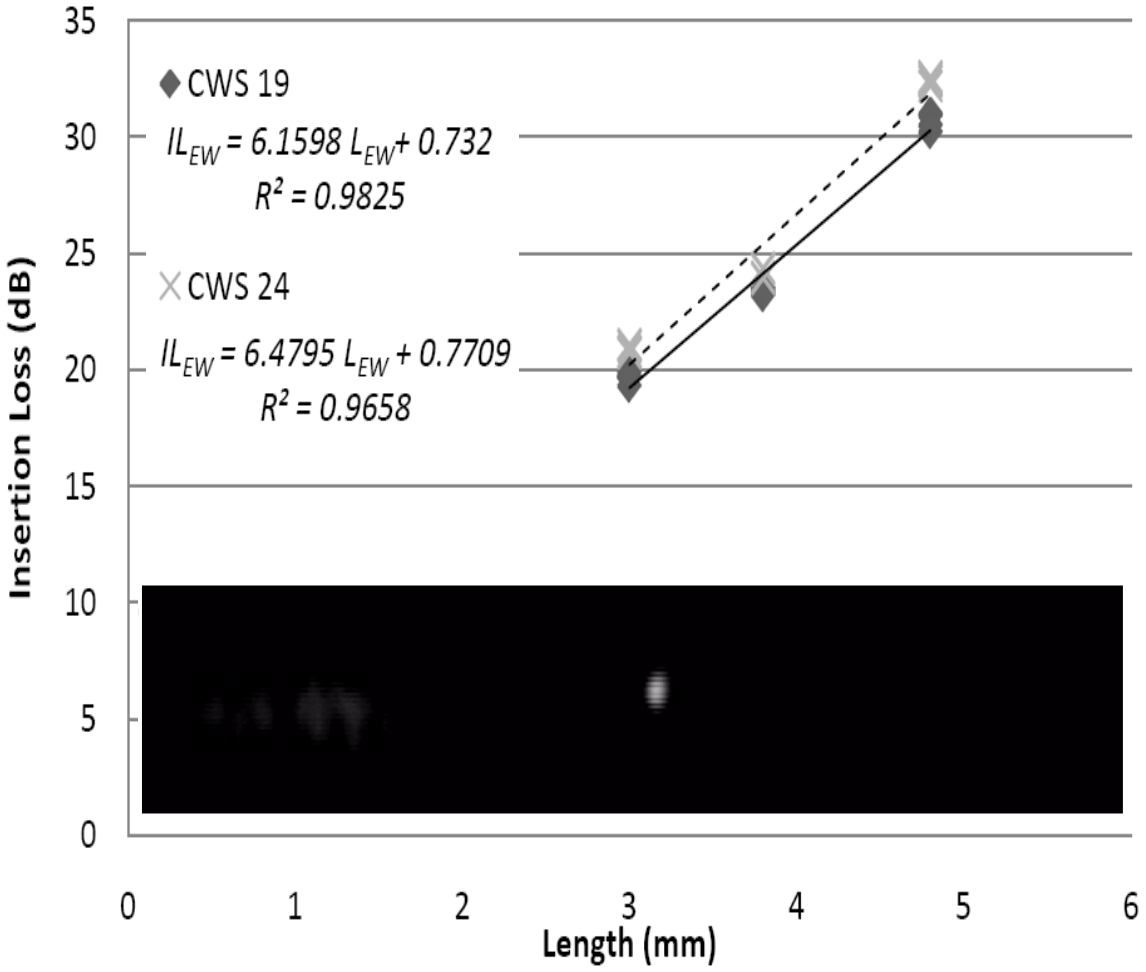

Figure 31: Cutback curve from CWS 19 and CWS 24 wafer respectively. Mode output from a waveguide selected from CWS 24 wafer.

Later on, a number of cladded waveguides retrieved from devices extracted from CLT13 wafer with a reported top cladding thickness of 9.49 nm and a bottom cladding of 10.4 nm respectively [32], were characterized. The results are presented in figure 32 which follows. The inset contains mode outputs from a single straight waveguide with a closed and an open aperture.

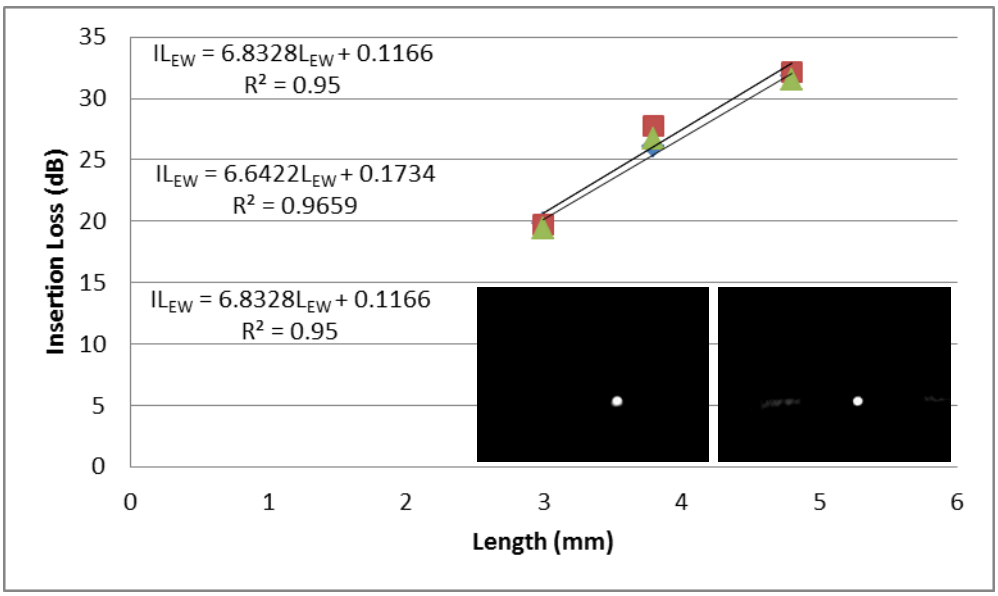

Figure 32: Cutback curve and mode outputs from CLT 13 wafer. The inset figures are of mode outputs with (open aperture) and without (closed aperture) radiation.

A number of wafers were prepared using an improved fabrication process in an effort to improve the quality of the waveguides by reducing surface roughness and gold spits. The process can be found outlined in [11]. One such wafer labelled ND-I was thoroughly investigated by obtaining DIEs of varying lengths from all quadrants of the wafer and characterizing them by using previously discussed means. These devices were interrogated by combining setup 3 and jig 3 previously discussed in chapter 3. A straight cladded waveguide from each device was selected for investigation. The results were found to vary significantly from one quadrant to the next, often with extremely high coupling losses. This was also evident from the mode profile with a high level of radiation surrounding the mode output. DIEs taken from top left quadrant of the wafer were deemed to be the most reasonable of all the characterization results obtained from other parts of the wafer. The MPA value was found to be 6.20 dB/mm and the coupling loss value was measured at 3.4 dB respectively. The chart in figure 33 below demonstrates the cutback curve as well as sample mode outputs obtained during the experimental process.

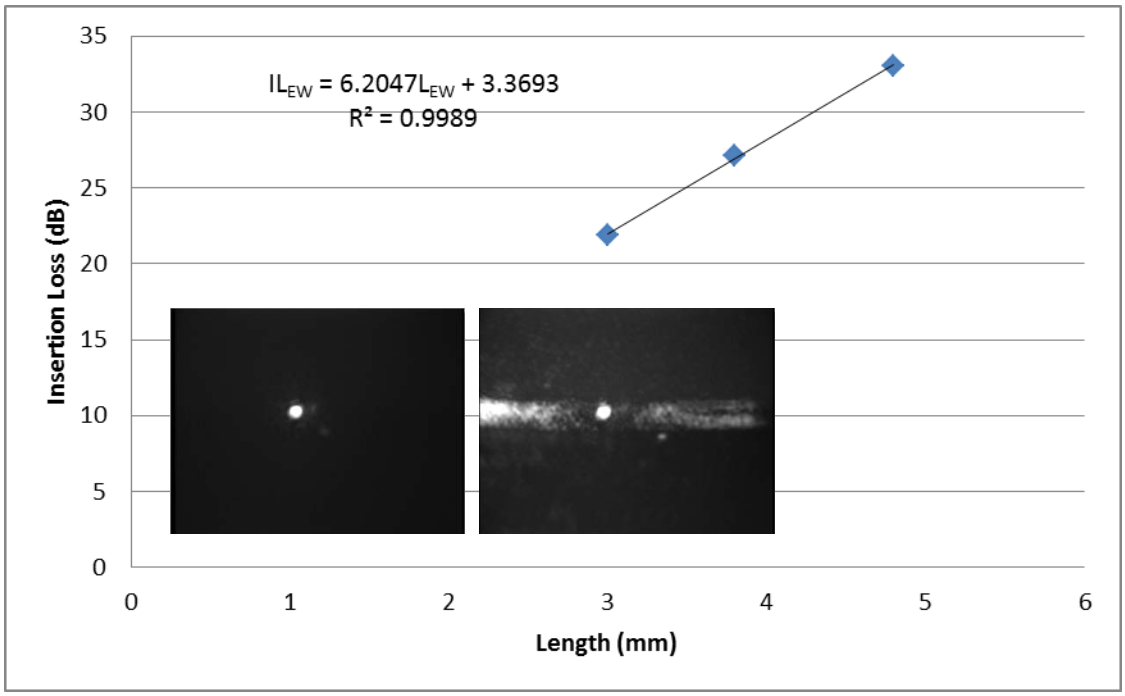

Figure 33: Cutback curve and mode output results from ND-I wafer. The inset figures are of mode outputs with (open aperture) and without (closed aperture) radiation.

Another wafer labelled ND-II from the same batch as the previous one was thoroughly investigated by obtaining DIEs of varying lengths from all quadrants of the wafer and characterizing them by using previously discussed means. These devices were also interrogated using a combination of setup 3 and jig 3. A straight cladded waveguide from each device was selected for investigation and the results were accumulated to draw an average MPA and coupling loss values which turned out to be ~ 6.0 dB/mm and 1.92 dB respectively. The chart in figure 34 below demonstrates the cutback curve as well as sample mode outputs obtained during the experimental process.

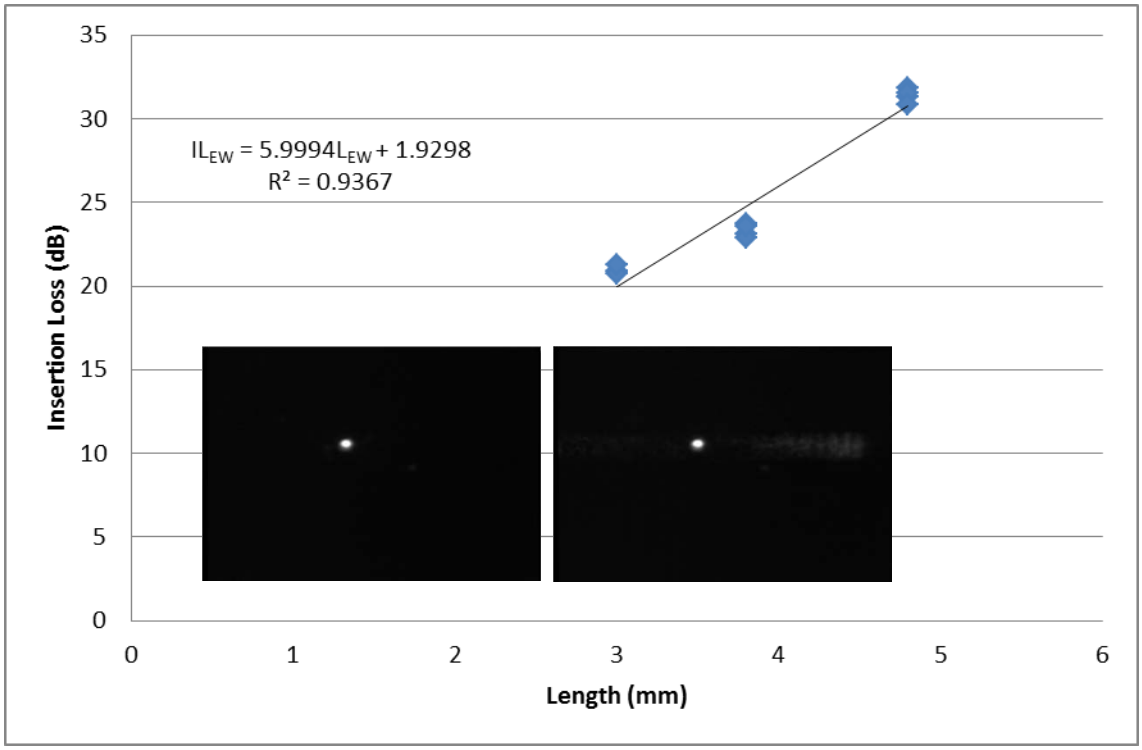

Figure 34: Cutback curve and mode output results from ND-II wafer.

6.3. Cladded waveguides with liquid filled etched channels:

From a bio-sensing stand point, it is critical to interrogate and characterize devices with etched channels which allow them to be filled with bio-sensing solutions for future applications envisioned for this project. Under ideal conditions, where the index matching fluid entering the etched channels would perfectly match the index of the bottom CYTOP cladding, the device would operate with losses comparable to those of a fully cladded device. With the refractive index of the sensing solution, ideally matched to that of CYTOP, the fluidic channels would disappear optically. The measured insertion losses are the collective account of losses incurred in both the cladded and the etched parts of the DUT.

In order to determine the loss of power associated with only the etched segments of the device, a number of measurements have to be carried out. First, the etched cavity length is subtracted from the total DIE length to determine the length of the embedded segment of the waveguide. Since the MPA of embedded waveguides is known from measurements carried out earlier (see previous sections), the loss associated with only the embedded regions is determined. This value is then subtracted from initial power calibration output, minus the coupling losses and the propagation losses of the embedded sections of the waveguide. The formula in equation 1 gives the detailed calculation for the insertion losses for partially etched straight waveguides.

$$IL_{CH} = P_{IN} - P_{OUT} - P_C - (P_{EW} \times L_{EW}) - \text{(Equation 4)}$$

Where IL_{CH} = Insertion Loss of filled channel waveguide
P_{IN} = measured Input Power from fiber
P_{OUT} = Power Output measured from device
P_C = Fiber-to-CYTOP Coupling loss (input & output facets)
P_{EW} = Mode Power Attenuation of Embedded Waveguide (MPA)
L_{EW} = Length of the Embedded Waveguide (millimeter)

Waveguides of varying lengths from a single wafer (CWS 24) were selected to extrapolate a power cutback curve which would help determine the MPA per millimeter of the device as well as the coupling losses at the end facets. The straight waveguides featured an etched channel over their surface which allowed for filling them with an index matching solution. The measured MPA of these devices was 10.46 dB/mm and the coupling loss per channel was evaluated to be 3.4 dB. The theoretical values obtained via simulation were 7.2 dB/mm and 0 dB respectively. Figure 35 which follows, demonstrates the cutback curves as well as a mode output in the inset.

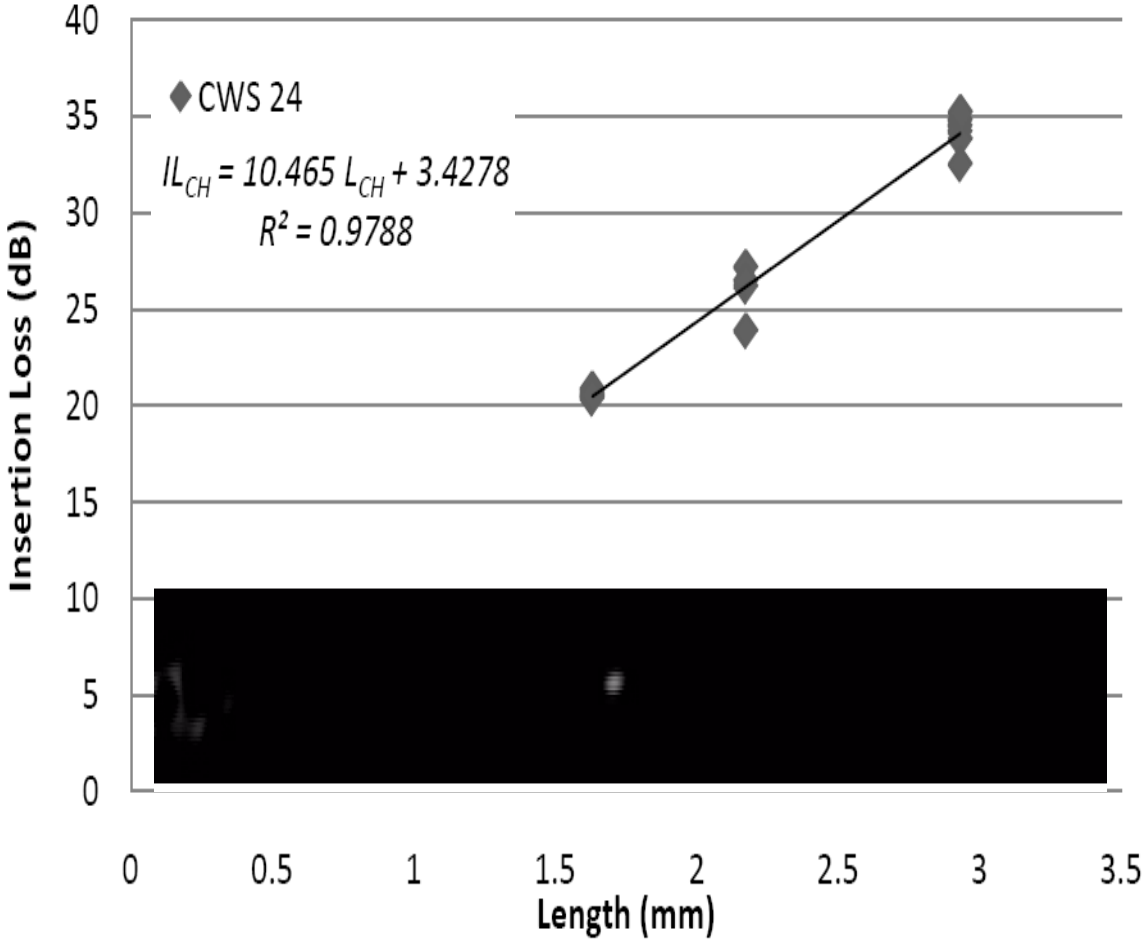

Figure 35: Cutback curve and mode power output derived from CWS 24 wafer.

The description of CWS 24 wafer device design and fabrication related details can be found in chapters 3 and 4 of [33]. Here it may be relevant to note that CWS24 and CWS13 wafers were both interrogated with a combination of Setup 2 and Jig 2 in place. The device interrogation process remained the same for the next set of measurements however the setup combination changed. A combination of Setup 3 with Jig 3, was utilized to test the wafers which follow.

Sample DIEs were acquired from wafer labelled Ct-Au-1 for optical characterization. 3 DIEs of varying lengths (3mm, 3.8 mm and 4.8mm) were selected from the wafer after careful microscope examination for surface irregularities and facet quality. The devices were then tested in the interrogation setup using index matched solution and the insertion losses were evaluated. The MPA values of 6.8 dB/mm and coupling losses of 1.9 dB were determined. The following chart along with the inset image, exhibits the cutback curve and a sample mode output obtained during the experimental process.

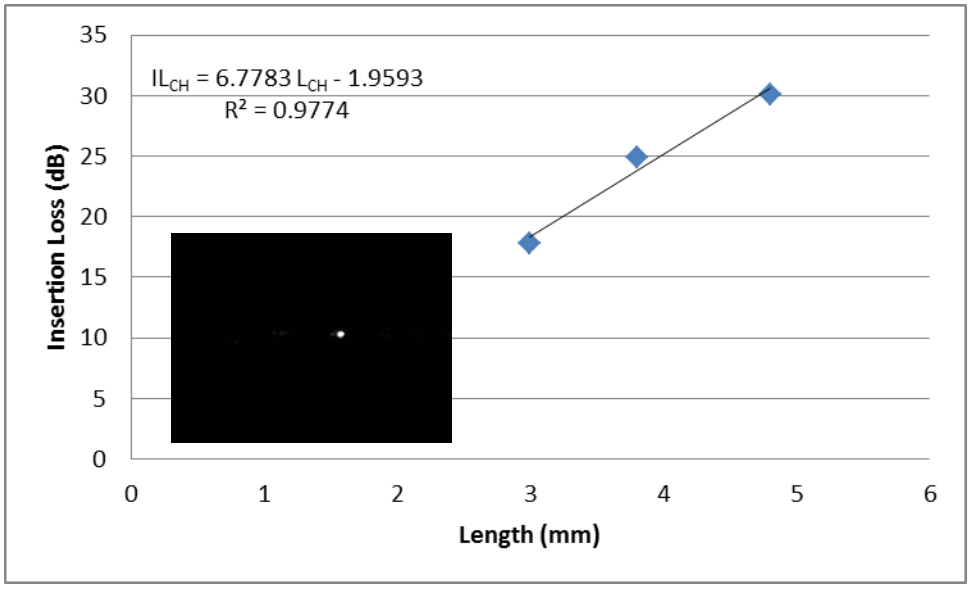

Figure 36: Insertion loss assessment and mode extraction from a waveguide selected on Ct-Au-1 wafer.

As evident from the data above, a number of wafers were characterized over the span of the study. These wafers consisted of waveguides of varying natures such as fully etched, fully cladded and partially etched (with either etched channels or etched segments exposing multiple waveguides) waveguides. The source of the wafers also changed over time as two different M.Sc. candidates prepared wafers following slightly differing protocols the details of which can be found

in [11] and [33].The characterization results from devices belonging a batch of wafers (referred to as Batch I Wafers) belonging to process flow employed in [11] are summarized in the table which follows:

Devices from Batch I Wafers						
Variable	Un-cladded Waveguides					
	Theoretical Value	CT-5 Wafer		CT-5 Wafer		
Attenuation (dB/mm)	7.2	7.37		7.57		
Coupling Loss per Facet (dB)	0.89	2.01		1.81		
Variable	Cladded Waveguides					
	Theoretical Value	CWS-19	CWS-24	CLT-13	CLT-13	CLT-13
Attenuation (dB/mm)	7.2	6.16	6.48	6.83	6.64	6.33
Coupling Loss per Facet (dB)	0.89	0.73	0.77	0.12	0.17	0.12
Variable	Partially Cladded Waveguides with liquid filled Channels					
	Theoretical Value	CWS-24				
Attenuation (dB/mm)	7.2	10.47				
Coupling Loss per Facet (dB)	0.89	3.42				

Table 4: Summary of characterization results of devices obtained from processes outlined in [36].

Characterization results from Batch II wafers, which are wafers obtained by following protocols entailed in [11] are summarized in the following table:

Devices from Batch II Wafers			
Variable	Cladded Waveguides		
	Theoretical Value	ND-I	ND-II
Attenuation (dB/mm)	7.2	6.20	3.36
Coupling Loss per Facet (dB)	0.89	5.99	1.92
Variable	Partially Cladded Waveguides with liquid filled Channels		
	Theoretical Value	At-Cu-1	
Attenuation (dB/mm)	7.2	6.78	
Coupling Loss per Facet (dB)	0.89	1.96	

Table 5: Summary of characterization results of devices obtained from processes outlined in [11].

6.4. Analysis:

6.4.1. Wafer CT-5

As described earlier, waveguides from CT-5 waveguides were tested for MPA and coupling loss values. The cutback curves generated exhibited a good linear fit in both cases (measurements were carried out for two sets of devices) and yielded MPA values of 7.37 dB/mm and 7.57 dB/mm respectively. These values compared reasonably well against the theoretical value of 7.2 dB/mm with the percentage error discrepancy of 2.4% and 5.1%. The coupling losses of 2.01 dB and 1.81 dB were reported and were compared against theoretically attained value of 0.89 dB. This was the only wafer tested which was completely bare (i.e. possessed no top cladding).

6.4.2. Wafers CWS 19 & CWS 24

The average MPA values as well as coupling losses values obtained by characterizing these wafers were found to be lower than the expected values reported in [34]. This was found to be the case because the thickness of the metal waveguides used in the wafers was thinner than the target of 35 nm. The AFM results obtained in [33] reported the metal surface to be curved instead of flat. The distortion in the metal surface is attributed to the cladding process where the solvent pressure caused the waveguide to bulge. Upon measuring the dimensions of the waveguides with CAD software and using the parameters obtained, the thickness of the waveguides was found to be 32.8 nm. A theoretical MPA value for the devices was than determined to be 6.40 dB/mm. This new value was found to be close to the average MPA value of 6.33 dB/mm. The lower coupling loss can be attributed to the wider waveguide stripe (5 µm) which is closely matched to the width of the fibre core (7 µm). This results in most of the light coupling into the waveguide therefore resulting in reduced coupling losses [36].

6.4.3. Wafer CLT-13

The mask used on this wafer allowed deposition of both fully cladded waveguides as well as waveguides with etched channels. The bottom cladding of the wafer was 10.4 µm and the top cladding was measured at 9.49 µm. As presented earlier in sections 6.1-6.3, 3 sets of measurements were collected and the average MPA value was determined to be 6.60 dB/mm. Once again the average value is found to be closer to the MPA value of 6.40 dB/mm associated with thinner waveguides as opposed to the theoretical value of 7.2 dB/mm.

6.4.4. Wafers ND I & ND II

As indicated by the data presented in Table 4, the experimentally determined attenuation values for the said wafers, were found to be lower than the theoretical values obtained using COMSOL [36]. This trend can be associated with the elimination of 'spits' on the gold as result of efforts undertaken to reduce overall deformation of the waveguides. On the other hand, higher coupling losses were observed compared to the theoretically reported values. One of the reasons for this could be insufficient cleaning of devices prior to optical testing. The devices returning from the dicing process are covered in a protective resist layer as well as residual debris from the dicing saw. This could compromise the quality of the facets. Coupling losses are highly sensitive to the alignment of the DUT with the interrogation fibre as well. A slight human error can cause deviation from theoretical values [11].

6.4.5. Wafer CWS 24

A number of devices were extracted from this wafer to extrapolate the cutback curve demonstrated in Figure. 34. The average attenuation and coupling loss of 10.47 dB/mm and 3.4 dB respectively, is determined. Both of these values are significantly higher than what the theory proposes. In theory, there should be no coupling loss between the waveguide embedded in CYTOP and the etched channel filled with index matched solution. In the presence of the solution, the channel should practically become invisible to the mode. One possibility for this loss is a mismatch between the solution and CYTOP despite the tweaking of the index with a temperature controller. The hydrophobic surface of CYTOP can also repel the solution from penetrating the channels effectively. This can result in formation of air gaps in corners between the raised devices within the channel and the CYTOP surface. Since the accumulated data was found to be fairly reproducible, it

can be deduced that the formation of air gaps could be a viable reason for the high MPA and coupling loss values [36].

6.4.6. Wafer At-Au-1

The aforementioned wafer had a 'snake etch' across the lateral length of its devices (ones used for optical characterization). These devices with a gold thickness of 34 nm were embedded between CYTOP claddings of 9 µm (lower) and 8 µm (upper) [11]. The recorded MPA value for the devices was 6.8 dB/mm and the coupling losses were measured to be 1.96 dB. The MPA values for these devices were found to be higher than the ones evaluated from previous devices belonging to the same batch (ND I and ND II). This could be explained by the fact that this wafer was fabricated using much of the old deposition process resulting in spits in gold adding to the surface roughness [11]. This raises the overall attenuation of the devices causing the MPA values to rise. The high coupling losses can once again be attributed to insufficient cleaning and improper fibre alignment with the DUT.

7. MZI Characterization Results:

As per the brief discussion in earlier chapters of this document entailing the Mach-Zehnder Interferometer (MZI) structure and its functional behavior, it is evident that the MZI is deemed a superior platform for sensing compared to devices consisting of straight waveguides (with or without etched channels) embedded in CYTOP which have been predominantly discussed thus far.

Part of the work done within the scope of this thesis, consisted of an effort to obtain characterization results of MZI devices. 2nd generation devices with side access channels for fluid delivery, were utilized for these set of measurements. The dies were obtained from a wafer labeled ND1 and consisted of two U-shaped cavities which were etched across the lateral length of the device, pointing away from each other. Each cavity spanned over half of the DIE length allowing index matching solution to enter from either end. The fluids entered from one end of the U-shaped cavity and exited from the other (see figure 37 below). A combination of Setup Design 3 and Jig Design 3 (both can be found in chapter 3 of this document) was used to interrogate these devices.

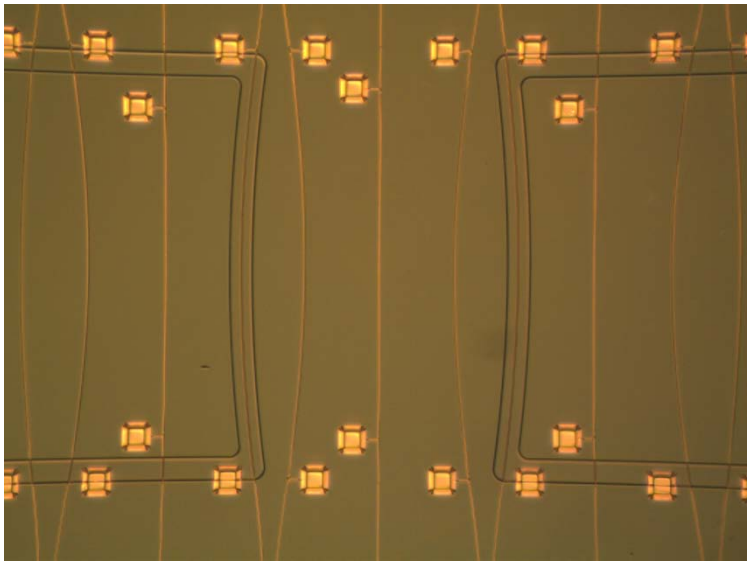

Figure 37: A second generation device with waveguides embedded in CYTOP showcasing side access channels across the lateral length of the device.

For a MZI structure, the power output is computed by using the following equation (also refer to figure 38):

- $P_{out}=(1/2)T_gP_{in}e^{-2\alpha(L_F+L_0)}W(1+V\cos(\phi_D))$ - (Equation 5)

Where:

- T_g is the power transmittance of the facets.
- P_{in} is the input power.
- P_{out} is the measured output power.
- L_F is the length of the fluidic channel.
- L_0 is the length of input and output path including splitter and combiner.
- α is the attenuation constant of the cladded waveguide

W is the power penalty due to excess losses incurred in the fluidic channel and is given by:

- $W=(T_F^2e^{-2\Delta\alpha L_F}+1)/2$ - (Equation 6)

Where:

- T_F is the transmittance at the cladded waveguide - fluidic waveguide interface.
- $\Delta\alpha$ is the difference between the attenuation of the fluidic channel and that of the cladded waveguide.

V is the visibility factor given by:

- $V=(2T_Fe^{-\Delta\alpha L_F})/(T_F^2e^{-2\Delta\alpha L_F}+1)$ – (Equation 7)

- ϕ_D is the difference in in the insertion phase between the sensing and reference arms given by:

  - $\emptyset_D=(2\pi L_F/\lambda_0)(n_{eff,F}-n_{eff})=(2\pi L_F/\lambda_0)\Delta n_{eff}=(2\pi L_F/\lambda_0)(\Delta n_c\partial n_{eff}/\partial n_c)+\phi_0$ – (Equation 8)

- ϕ_0 is the nominal (residual) phase difference between the arms.
- λ_0 is the interrogation wavelength.
- n_c is the index of the sensing fluid and Δn_c is a change in this index.
- $n_{eff,}$ and $n_{eff,F}$ are the effective indices of the cladded waveguide and of the waveguide within the fluidic channel filled with a solution of index n_c

$\partial n_{eff}/\partial n_c$ is the bulk sensitivity of the waveguide.

To arrive at P_{out} given by equation 1, the E-field associated with the LRSPP inside the die (E_{out}) must be considered; E_{out} is given by the following equation:

$E_{out} = E_{in}\, e^{-\alpha L_0} (1/\sqrt{2})(1/\sqrt{2})(\sqrt{T_F})(\sqrt{T_F})\, e^{-\alpha_F L_F} e^{-j\phi_F} + (1/\sqrt{2})(1/\sqrt{2})\, e^{-\alpha L_F} e^{-j\phi_R}$ – (Equation 9)

Where:

- ϕ_F is the insertion phase of the arm within the fluidic channel
- ϕ_R is the phase of the reference arm

Equation 5 can be rewritten as:

$E_{out} = E_{in}\, ½\, e^{-\alpha L_0} (T_F\, e^{-\alpha_F L_F} e^{-j\phi_F} + e^{-\alpha L_F} e^{-j\phi_R})$ – (Equation 10)

The complex conjugate of the above equation is given as:

$E^*_{out} = E^*_{in}\, ½\, e^{-\alpha L_0} (T_F\, e^{-\alpha_F L_F} e^{j\phi_F} + e^{-\alpha L_F} e^{j\phi_R})$ – (Equation 11)

P_{out} can then be given by the following equation:

$P_{out} = E_{out}E_{out}^* = P_{in}\, ¼\, e^{-2\alpha L_0} (T_F^2\, e^{-2\alpha_F L_F} + T_F\, e^{-\alpha_F L_F} e^{-\alpha L_F} e^{-j\phi_F} e^{j\phi_R} + T_F\, e^{-\alpha_F L_F} e^{-\alpha L_F} e^{j\phi_F} e^{-j\phi_R} + e^{-2\alpha L_F})$ – (Equation 12)

Equation 8 can be rewritten as:

$P_{out} = P_{in}\, ¼\, e^{-2\alpha L_0} (T_F^2\, e^{-2\alpha_F L_F} + e^{-2\alpha L_F} + T_F\, e^{-(\alpha_F + \alpha) L_F} e^{j(\phi_F - \phi_R)} + T_F\, e^{-(\alpha_F + \alpha) L_F} e^{j(\phi_F - \phi_R)})$ – (Equation 13)

$P_{out} = P_{in}\, ¼\, e^{-2\alpha L_0} (T_F^2\, e^{-2\alpha_F L_F} + e^{-2\alpha L_F} + e^{-2\alpha L_F} + e^{-2L_F} + 2T_F\, e^{-(\alpha_F + \alpha) L_F} \mathrm{Cos}(\phi_F - \phi_R)$ – (Equation 14)

where $(\phi_F - \phi_R)$ is defined as ϕ_D. (Equation 5).

Solving equation 10 further leads to:

$P_{out} = P_{in}\, ½\, e^{-2\alpha L_0} [(T_F^2\, e^{-2\alpha_F L_F} + e^{-2\alpha L_F} / 2) + T_F\, e^{-(\alpha_F + \alpha) L_F} \mathrm{Cos}(\phi_D)]$ – (Equation 15)

$P_{out} = P_{in}\, ½\, e^{-2\alpha L_0} [(T_F^2\, e^{-2\alpha_F L_F} + e^{-2\alpha L_F} / 2)\, (1 + 2T_F\, e^{-(\alpha_F + \alpha) L_F} / T_F^2\, e^{-(\alpha_F L_F} + e^{-2\alpha L_F}) \mathrm{Cos}(\phi_D)]$ – (Equation 15)

Let $\alpha_F - \alpha = \Delta\alpha$, therefore $\alpha_F = \alpha + \Delta\alpha$

Rewrite equation 15 as:

$P_{out} = P_{in}\, ½\, e^{-2\alpha L_0} [(T_F^2\, e^{-2(\alpha+\Delta\alpha) L_F} + e^{-2\alpha L_F} / 2)\, (1 + 2T_F\, e^{-(\alpha + \Delta\alpha + \alpha) L_F} / T_F^2\, e^{-(\alpha+\Delta\alpha) L_F} + e^{-2\alpha L_F}) \mathrm{Cos}(\phi_D)]$ – (Equation 16)

$P_{out} = P_{in}$ ½ $e^{-2\alpha L_0}$ $e^{-2\alpha L_F}$ $[(T_F^2\, e^{-2(\alpha+\Delta\alpha)L_F} + e^{-2\alpha L_F} / 2)\ (1 + 2T_F\, e^{-(\alpha+\Delta\alpha+\alpha)L_F} / T_F^2\, e^{-(\alpha+\Delta\alpha)L_F} + e^{-2\alpha L_F})\ \mathrm{Cos}(\phi_D)]$ – (Equation 17)

The power penalty (W) described in equation 6 and the visibility factor (V) from equation 7, can now be appropriately substituted in equation 17 to yield equation 5.

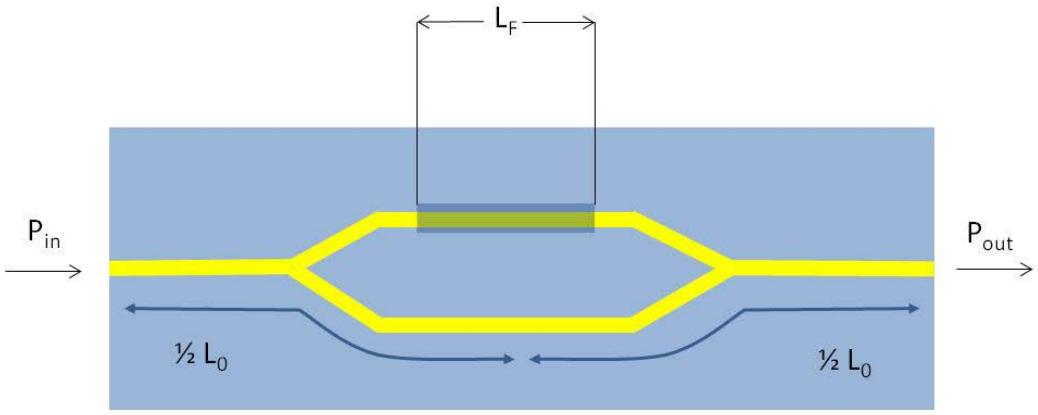

Figure 38. Schematics of MZI configuration illustrating key variables employed for P_{out} computation.

The MZI structures were used to determine the changes in the output power corresponding to variations in the refractive indices of a range of solutions. Ten solutions (ranging from a refractive index of 1.329 to 1.33044 with an index increase of 0.00016) were sequentially injected in the DUT obtained from the wafer labeled ND1with a lower cladding thickness of 9 μm and an upper cladding thickness of 8 μm. A waveguide, approximately 34 nm thick and of length 3.8 mm was tested and the power output corresponding to a refractive index solution, was measured on the photo detector. Theoretical power output values were computed and then plotted against their corresponding refractive index values. The curve obtained was then compared against the curve consisting of the experimentally determined power values plotted against the refractive index range.

The theoretical values derived from equation 1 rely on MPA as well as coupling loss values associated with both cladded and etched waveguides. In an effort to keep things consistent, MPA and coupling loss values were obtained by characterizing a set of both cladded and etched devices of varying lengths. The same procedure was followed to characterize a set of cladded devices obtained from the ND1 wafer, as the one entailed in chapter 6 of this document. The following cut back curve (figure 39) was obtained by Ewa Lisicka using an input fibre of 7 µm diameter and using an interrogation wavelength of 1310 nm. Index matching fluid was used between the input facet of the chip and the optical fibre to ensure optimal results. As always devices of 3 varying lengths were optically interrogated yielding a coupling loss at the input facet of 0.5539 dB and an MPA value of 6.0697dB/mm respectively.

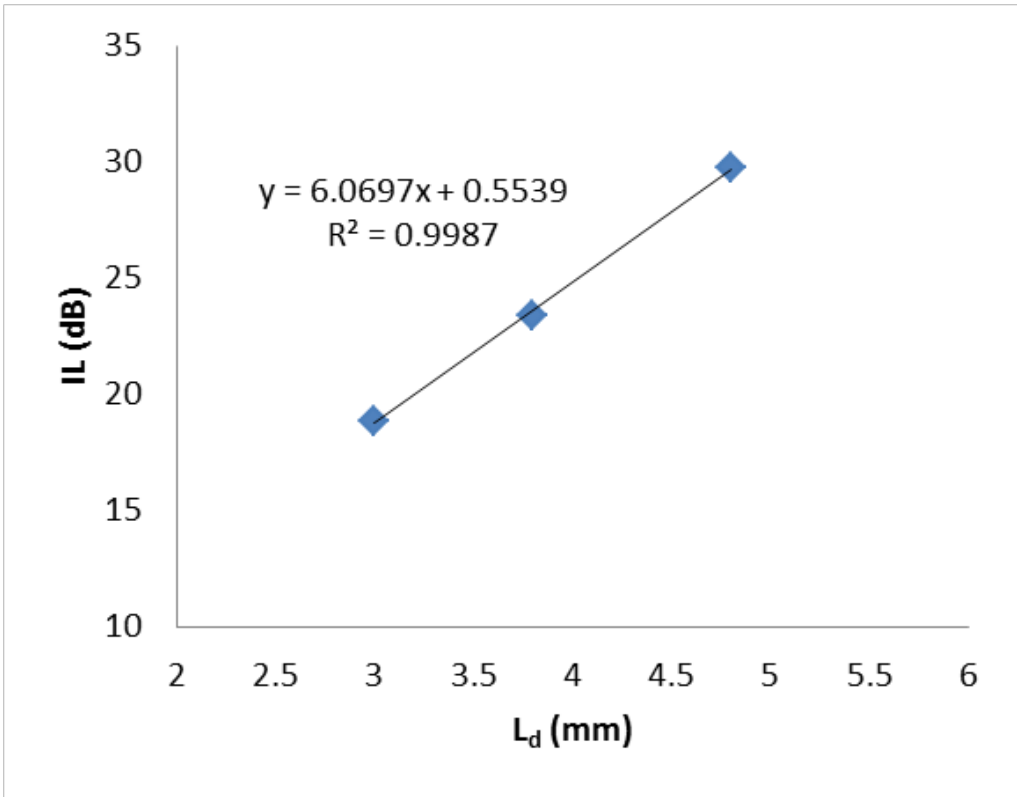

Figure 39: Cutback curve for fully cladded waveguides of 3 lengths obtained from ND-I wafer.

The cutback curve for fluidic channels was obtained by following the procedure outlined in section 6.3 of this document. A single waveguide with a 'snake' etched over the devices exposing varying lengths of the waveguide was used to obtain the cutback curve found in figure 40. Coupling losses of 3.7214 dB at the input and output of the fluidic channels as well as an MPA value of 8.8796 dB/mm were obtained (see figure 39). The channels were filled with a buffer and glycerol solution mixture with a measured refractive index of 1.3303.

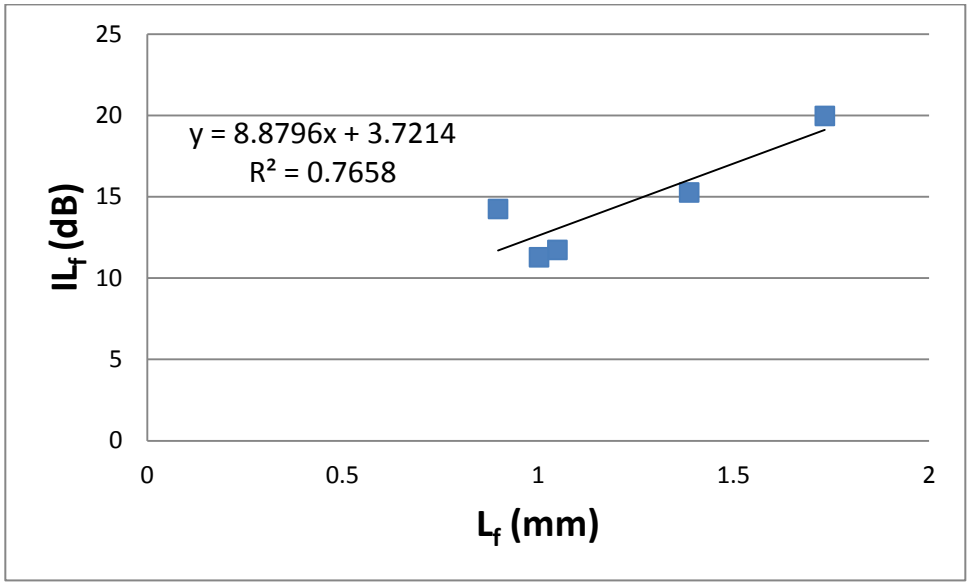

Figure 40: Cutback curve of fluidic channels of varying lengths obtained from a Die with a snake etch, yielding coupling losses of 3.7 dB at the input and output end of the etched channel and an MPA of 8.88 dB/mm.

The following chart (figure 41) is a comparison between the theoretically obtained curve and the curve consisting of experimentally determined values for the MZI:

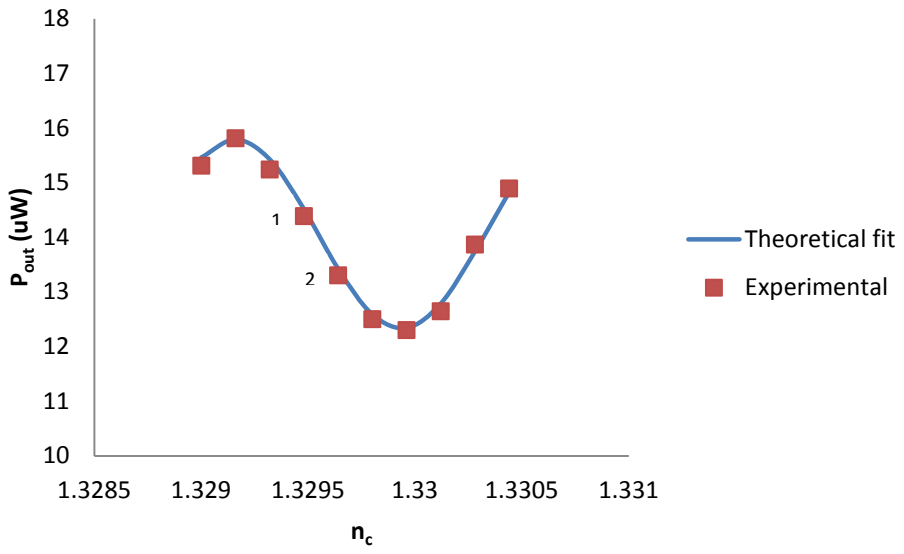

Figure 41: Theoretical vs. Experimental curve of MZI responses as solutions of varying refractive indices are sequentially injected into fluidic channels. (Data points 1 and 2 were selected to determine the limit of detection later in the chapter).

In order to correlate with the experimentally determined curve, the theoretical curve had to be fitted using the MZI equation (see equation 5) and by using a fitting factor of 0.827 for the cladded waveguide attenuation, a fitting factor of 0.5 for the input facet transmittance and a fitting factor of 1.7 for the attenuation of the fluidic waveguide. The values reported in figure 39 and 40, were used as the nominal values for the calculations.

Choosing the fitting factor of 0.827 to adjust the cladded waveguide attenuation can be justified, because though at 5.0196 dB/mm (0.827 x 6.0697) it yields lower than previously determined attenuation values, such attenuation has been observed on other wafers (note the attenuation variation reported for wafer CT-5 and ND II at 7.57 dB/mm and 3.36 dB/mm respectively in tables 4 and 5). The fitting factor of 1.7 for the fluidic waveguides yields an attenuation value of 15.095 dB / mm. This higher than expected attenuation can be attributed to a refractive index value of the solutions used in the experiment, which is lower than what is required

to optimally match the refractive index of CYTOP. Another cause for the higher attenuation could be imperfections in the waveguide and non-ideal fabrication processes.

For the theoretical data reported in [8] the following limit of detection for MZIs in dielectric-metal-dielectric configurations has been reported: for $\lambda_0 = 1310$ nm, $\Delta\Gamma_{min} = 0.25$ pg/mm^2. (where $\Delta\Gamma$ – minimum detectable mass, i.e. sensitivity). As a comparison, the theoretical detection limit for conventional SPR sensors is 1.0 pg/mm^2 [40]. Along with the same advantages as in SPR (label-free, real-time), a 4-5 times lower detection limit makes MZI LRSPP very appealing and promising for biosensing investigation.

Experimental limit of detection (LoD) for bulk change was determined from the data reported in figure 41. The bulk sensitivity detection can be extracted by selecting two points from the linear region of the sinusoidal wave and the LoD is calculated by $\partial P_{out}/\partial n_c$. For the bulk change of 10^{-4} RIU (refractive index units), a corresponding response of 1.0834μW (where the bulk change and the response values are both extracted from the data points selected from figure 41) and a baseline noise of $2\sigma = 9.71$nW (where the noise corresponds to the baseline noise of the setup) yields a LoD of 8.96×10^{-7}RIU.

8. Surface Biosensing:

Another goal of thesis project was to characterize this optical platform that will ultimately act as bio-sensors devised to investigate presence of biological entities in a given sample. An experiment was carried out using Au waveguides embedded in CYTOP with micro-fluidic channels etched over the waveguides. The top cladding necessary for surface plasmons to propagate was formed by a glycerol/water solution index matched to CYTOP in order to support a high quality mode from a straight etched waveguide. A range of solutions with varying refractive indices, were prepared in a bid to test and find one which was an optical match for the refractive index of CYTOP, details of which can be found in section 5.3 (Bulk Sensing Measurements).

The potential for straight waveguides to detect whole cells was investigated in this experiment. Certain pathogenic strains of *E-Coli* are known to cause health issues of serious nature with high costs associated with treatment and prevention of illnesses that the said strains are known to incur. Currently a number of techniques are used in practice to detect these bacteria, some of which are: PCR, ELISA, piezoelectric biosensors, amperometric sensors, bioluminescence, fluorescent labelling and SPR [37]. In this study, an experiment was conducted to examine the general response of a waveguide to the binding of cells on the surface. A simple interaction between E-coli XI-1 Blue stock and antibodies against Gram negative bacteria (Anti-Gneg) was used for this proof of concept.

A combination of setup 2 and jig 2 (described in detail in chapter 3) was employed to investigate the bio-sensing waveguides used in this experiment. The devices were prepared by washing the photoresist off the DIEs after they returned from dicing. This was accomplished by soaking DIEs in pure acetone for 20 minutes followed by a quick rinse in acetone after which the

DIEs were quickly immersed in IPA (iso-propyl alcohol) for another 10 minutes. After this step, the devices were rinsed with distilled/deionized water (DI H_2O) and dried with nitrogen. The devices were further exposed to UV light and UV generated ozone for further cleaning.

The cleaning process was followed by surface functionalization which saw the devices immersed in a carboxyl-terminated alkanethiol 16-MHA (16-mercaptohexadecanoic acid, 2 mM in IPA) solution, immediately after the UV ozone treatment, for 20 hours. This was done to facilitate the formation of a self-assembled monolayer (SAM) on the surface of the exposed waveguides. After incubation, the devices were rinsed with IPA and DI H_2O once again and dried. The activation of carboxyl groups was done by 0.1 M EDC [N-(3-Dimethylaminopropyl)-N'-ethylcarbodiimide hydrochloride] /NHS [N-Hyrdroxysuccinimide sodium salt] (1:1)[38] in DI H_2O for 15 minutes in a vial after which the devices were rinsed with water and then placed in a vial containing 0.5 mg/ml Anti-Gneg in PBS (the anti-bodies against *E.Coli* Xl-1 Blue bacteria strand). The antibodies were allowed to react with the surface for 2 hours. After this incubation period, the devices were thoroughly rinsed with PBS and the unreacted sites were blocked by using 0.1 M glycine in PBS solution, for 10 minutes.

The gram negative bacteria were prepared for the experiment by using a small aliquot of *E.Coli* Xl-1 Blue stock and diluting it in 5 ml of PBS solution. The colonies were allowed to grow in a petri dish for 16 hours at 37°C. A few of these colonies were diluted in 2 ml PBS and washed three times in a centrifuge with index matching glycerol/water solution (4000 rpm for 2 minutes). Cells were counted using a hemacytometer chamber. The cell concentration was found to be 10^{10} cells/ml of the solution.

The DUT was positioned in the jig such that it sat snug within the etched groove on the jig. An optical fibre was butt coupled into a straight etched waveguide in order to obtain a high quality

mode output. A wavelength sweep ranging from 1265 to 1350 nm was carried out with waveguides with only functionalized antibodies on their surface. The Anti-Gneg functionalized die was then exposed to the *E.Coli* solution until a drop in signal was observed. The remaining cells were washed away using PBS at a flow rate of 20 µL/min. A subsequent wavelength sweep employing the same wavelength range was carried out after the solution with bacteria was washed over the device and the two sweep results were compared to determine measureable change in the response of the waveguide as a result of bacteria binding to the antibodies. The output power over two wavelength sweeps are compared in figure 42 to emphasize changes in waveguide insertion loss due to the presence of bacteria bound to the exposed waveguide surface.

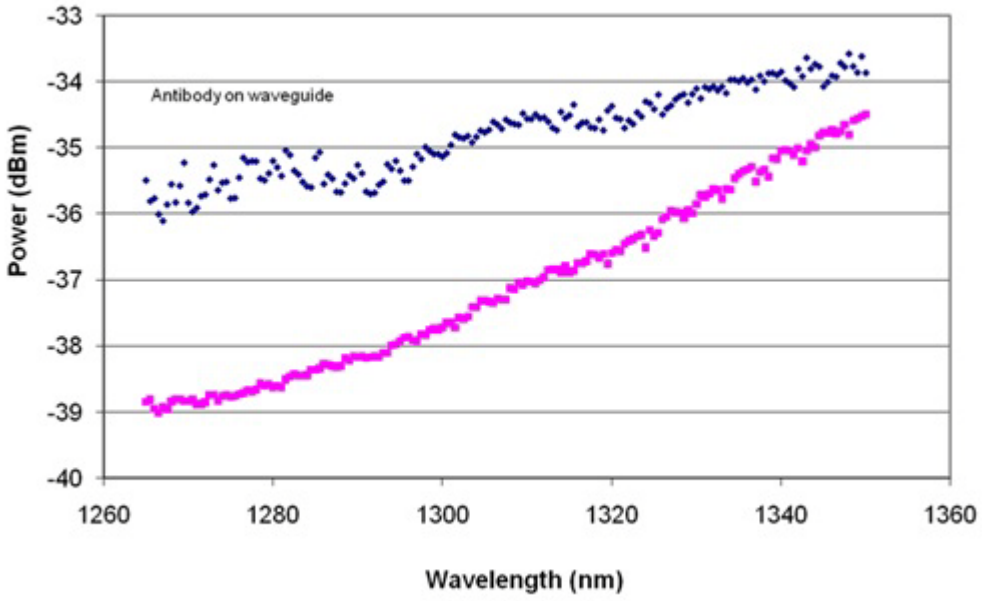

Figure 42: Wavelength response of straight waveguides coated with antibodies on SAM, without bacteria (top trace) and with 9 bacteria (bottom trace).

The difference in output power levels between the two waveguides is very pronounced near 1265 nm; however the difference begins to narrow as the sweep continues to longer wavelengths. When carrying out wavelength sweeps, it was important to strike a balance between the power levels obtained from the mode output and the amount of radiation surrounding the mode when subjected to various wavelengths. It was experimentally determined that at 1310 nm, the mode exhibited little to no radiation all the while maintaining enough sensitivity to showcase any power variation associated with binding events. For this experiment (Fig. 42, at 1310 nm), a 3 dB increase in insertion loss was measured for a waveguide coated by 9 bacteria relative to a waveguide devoid of bacteria (only coated with antibodies) [39]. The bacteria count was done by disassembling the DUT enclosure and examining the device under microscope set to a 100x magnification.

9. Conclusions and Future Work:

This thesis lays an extensive focus upon interrogation and characterization of integrated LRSPP biosensing platforms consisting of gold waveguides embedded in CYTOP. A number of wafers fabricated utilizing a variety of fabrication processes, were investigated using optical probing to evaluate the quality of the devices and their biosensing capabilities. Characterization results for fully embedded gold waveguides in CYTOP, fully exposed (etched) waveguides and partially exposed waveguides (with channels) were reported. Both straight waveguides and MZI structures were investigated. A number of power cutback curves were generated to determine the MPA and coupling loss characteristics for a number of device batches. Theoretical mode power attenuation (MPA) value of 7.2 dB/mm was sought in all cases and though the requirement was not exactly met, the experimentally determined values consistently hovered close to the expected values (see table 4 and 5). Coupling losses on the other hand, remained consistently higher. These shortcomings can be attributed towards inconsistencies in waveguide characteristics (thickness, surface roughness etc), variations in refractive index of optical solutions used to match the refractive index of CYTOP, stability of the interrogation setup and human error while carrying out setup alignment procedures.

The thesis also documented the evolution of the optical interrogation setup over the span of the study. As a varying number of device layouts and geometries came about and were tested, a need to consistently upgrade and improve the setup to keep up with the requirements of the experiments remained persistent throughout. The steps taken to improve and simplify the setup in an effort to remain practical and more importantly, stable over time, were reported in this thesis. The jig design also evolved alongside changes in the device design to address needs such as: the accessibility of the probing fibre to the waveguide facet, delivery of the index matched solution in

and out of the device, suitable encapsulation of the solution within the device channels without leaking outside the jig, and easy observation of the device during the experimental process.

Another aspect of the thesis was to validate the importance of the index matching solution used in tandem with exposed waveguides. A section dedicated to bulk sensing was included to explain the effect of proper index matching on the mode output quality as well as the effect on the output power with variations in the refractive indices of subsequently injected solutions in the DUT.

Results of MZI interrogation are also reported in this document. MZIs from second generation devices consisting of waveguides with side access channels were interrogated using the most recent combination of interrogation setup and device jig. A range of solutions were sequentially injected and their power outputs were monitored. The values were plotted against each other and were compared against a theoretical fit. Arbitrary factors were chosen to fit the experimental curve to the theoretical one. The fitting factor of 0.827, chosen to match the waveguide attenuation was consistent with previously determined attenuation values. The fitting factor of 1.7 yielded a significantly higher attenuation for the fluidic guides, a phenomenon observed as a result of fabrication imperfections and discrepancies in refractive index matching.

With the continuous improvements in device fabrication methods and techniques documented in [11] and [33] along with the enhancement of the bio-sensing devices and their designs, the need for the characterization methods to keep up will remain a pressing challenge. A number of issues stated above will have to be addressed going forward. For starters, there is room for improvement in the stability of the interrogation setup. As of now, by mounting the multi axis stages on a floating optical table, they are isolated from vibrations to a considerable extent. The stages themselves do a fair job of remaining steady over a period of time. However, during particularly long experimental episodes, a slight drift in the stages has been observed. The latest

stages are capable of both manual and piezoelectric controlled operation however during the span of this thesis, the stages were only put to use in manual mode. Future experimentation can be carried out utilizing the precision offered by the piezoelectric option. A cardboard enclosure supplemented with a thick, dark cloth, has been used to encase the interrogation platform in a bid to isolate it from wind drafts that might disturb the positioning of the optical fiber. The enclosure itself can be improved upon by selecting a sturdier build material other than cardboard. The variations in the refractive index solution can be mitigated in the future experiments, in a bid to reduce errors further. This can be achieved by acquiring more precise instrumentation involved in the measurement and mixing of index solutions.

The evolution of the fabrication process has promised a new generation of devices which include a glass lid laid over the devices to form pre-encapsulated channels, effectively eliminating the need to devise elaborate jigs to contain the index matching solutions as it flows in and out of the device channels. If effectively realized, these devices will simplify the process of optical interrogation and the delivery as well as extraction of the bio sensing solutions, significantly. Possible future work can include interrogation of these promising platforms.

The research work documented here has also been reported in proceedings papers a number of times. A paper titled “Characterization of Biosensing Waveguides on Cytop”, has been part of the proceedings for NanoONTARIO 2010 - Ontario Nanoscience and Nanotechnology Workshop held at University of Western Ontario, London, Canada in May 2010 and followed by a publication for the proceedings of SPIE Photonics North conference held at Niagara Falls, Canada in June 2010. Another paper titled “Sensing of bacteria immobilised under static conditions using long-range surface plasmon waveguides in Cytop”, was a part of SPIE Photonics North proceedings held at Ottawa, Canada in May 2011. Furthermore, the research work here has contributed to a paper

titled “Fabrication of surface plasmon waveguides and integrated components on Cytop”, published b y (Elsevier) Microelectronic Engineering, Vol. 87 in 2010. A proceedings paper titled “Fabrication of Surface Plasmon Waveguides in Cytop” for the SPIE Photonics North conference: CIPI, held at Montréal, Canada in June 2012 has also quoted some of the work reported here. A proceedings paper titled “Long-Range Surface Plasmon Polariton (LRSPP) waveguides as a platform for blood group immunophenotyping”, for Nano-ONTARIO 2011 - Ontario Nanoscience and Nanotechnology Workshop held by McMaster University, Hamilton, Canada, on May 2011, also contains contributions from the research work reported here. A poster titled “Characterization of Biosensing Waveguides in CYTOP” has been presented at Biopsys, a strategic network for Bioplasmonic Systems aimed at improved prognosis and shorter diagnosis time for cancers, funded by NSERC.

In addition to all the contributions listed above, another publication for a reputable journal such as Journal of Applied Physics or Journal of Vacuum Science and Technology is also in the works. This paper will likely include fabrication and validation work related to the MZI structures that have been reported in chapter 7 of this document.

10. References:

[1] D. Mathers, C. Colin, C. Boschi-Pinto, A. D. Lopez and C. J.L. Murray, Cancer incidence, mortality and survival by site for 14 regions of the world, Global Program on Evidence for Health Policy Discussion ed. , Paper No. 13 : World Health Organization, 2001.

[2] Y. Yeo-Heung, B. Amit, W.B. Nelson and S. J. Mark, A Label-Free Electronic Biosensor for Detection of Bone Turnover Markers, 9 ed. , 7957-7969: Sensors (Basel), 2009.

[3] Z. Yi-Hua, H. Tse-Chao and X. Fei. , IEEE-EMBS 27th Annual International conference proceeding, Engineering Medicine and Biology Society ed. , 1909-1912: Conference Publication, 2005.

[4] P.N. Prasad, Introduction to Biophotonics, John Wiley and Sons Inc, 2003.

[5] R.S. Marks, Handbook of biosensors and biochips, Vol. 1 ed. , John Wiley and Sons Inc, 2007.

[6] A.J. Killard, B. Deasy, R. O'Kennedy, and M.R. Smyth, Antibodies: production, functions and applications in biosensors, 14 ed. , 257-266: TrAC, Trends Anal. Chem, 1995.

[7] K. Motesharei and D.C. Myles, Molecular Recognition on Functionalized Self-Assembled Monolayers of Alkanethiols on Gold, 120 ed. , 7328-7336: Journal of The American Chemical Society, 1998.

[8] P. Berini, Bulk and surface sensitivities of surface plasmon waveguides, 10 ed. , 105010: New Journal of Physics, 2008.

[9] R. Narayanaswamy and O.S. Wolfbeis, Optical Sensors, Springer, New York, 2004.

[10] X. Fan, I. M.White, S. I.Shopova, H. Zhu, J.D.Suter, Y.Sun, Sensitive optical biosensors for unlabeled targets: A review, 620: Analytica Chimica Acta , 2008.

[11] H. Asiri, Fabrication of Surface Plasmon Biosensors in CYTOP, M.Sc. Thesis ed. , University of Ottawa, 2012.

[12] O. Krupin, Biosensing using long-range surface plasmon polariton (LRSPP) waveguides, Ph.D. thesis proposal ed. , Univeristy of Ottawa, 2011.

[13] D.G. Castner, C.B. Duke, E.W. Plummer and B.D. Ratner, Frontiers in Surface and Interface Science, Amsterdam: North-Holland: 2002.

[14] F. Schreiber , Prog. Surf. Sci, 16 ed. , 881: J. Phys.: Condens. Matter, 2004.

[15] E. Ostuni, et al, A Survey of Structure-Property Relationships of Surfaces that Resist the Adsorption of Protein, 17 ed. , 5605-5620: Langmuir, 2001.

[16] R.W. Wood, Philos. Mag, 4 ed. , 396-402: 1902.

[17] R.W. Wood, Philos. Mag, 23 ed. , 310-331: 1912.

[18] U.J. Fano, Opt. Soc. Am, 31 ed. , 213-222: 1941.

[19] A. Otto, Z. Phys, 216 ed. , 398–410: 1968.

[19] E. Kretschmann, H. Reather and Teil A, Introduction to Surface Plasmon Resonance, 136 ed. , 2135–2136: 1968.

[21] J. Homola, Surface Plasmon Resonance Sensors for Detection of Chemical and Biological Species, 108(2) ed. , 462-493: Chemical Reviews, 2008.

[22] D. R. Shankaran, V. Gobi, and N.Miura, Recent advancements in surface plasmon resonance immunosensors for detection of small molecules of biomedical, food and environmental interest, B, 121 ed. , 158–177: Sensors and Actuators , 2007.

[23] I. Abdulhalim, Enhancing the sensitivity of surface-plasmon resonance sensors, DOI: 10.1117/2 ed. , 1200901.1466: SPIE Newsroom, 2009.

[24] D. R. Shankaran, V. Gobi, and N. Miura, Recent advancements in surface plasmon resonance immunosensors for detection of small molecules of biomedical, food and environmental interest, B. 121 ed. , 158–177: Sensors and Actuators , 2007.

[25] X.C. Yuan, B. H. Ong, Y. G. Tan, D. W. Zhang, R. Irawan, and S. C. Tjin, Sensitivity-stability-optimized surface plasmon resonance sensing with double metal layers, Opt. 8 ed. , 959-963: J. Opt. A–Pure Appl. , 2006.

[26] W. Bin and W. Qing-Kang, High sensitivity transmission-type SPR sensor by using metallic dielectric mixed gratings, Lett. 25 ed. , 1668–1671: Chin. Phys. , 2008.

[27] C. J. Alleyne, A. G. Kirk, R. C. McPhedran, N. A. P. Nicorovici, and D. Maystre, Enhanced SPR sensitivity using periodic metallic structures, 15 ed. , 8163–8169: Opt. Express , 2007.

[28] P. Berini, Charbonneau, R., Lahoud, N., Mattiussi, G. , Characterization of long-range surface plasmon polariton waveguides, Vol. 98 (1), 043109 ed. , 1-12: Journal of Applied Physics, 2005.

[29] P. Berini, Plasmon-polariton waves guided by thin lossy metal films of finite width: Bound modes of symmetric structures, Vol. 61 ed. , 10484: Physical Review B, 2004.

[30] B. Sepúlveda, J. Sánchez del Río, M. Moreno, F. J. Blanco, K. Mayora, C. Domínguez and L. M. Lechuga , Optical biosensor microsystems based on the integration of highly sensitive Mach–Zehnder interferometer devices, Vol. 8 ed. , S561: J. Opt. A: Pure Appl. Opt, 2006.

[31] A. Densmore, D.X. Xu, P. Waldron, S. Janz, A. Delâge, P. Cheben and J. Lapointe, Thin silicon waveguides for biological and chemical sensing, Vol. 6477 ed. , 647718: Proc. of SPIE, 2007.

[32] A. Ulman , Chem. Rev, 96 ed. , 1533: 1996.

[33] C. Chiu, Fabrication of surface plasmon waveguide devices in CYTOP with microfluidic channels, M.A.Sc. Thesis ed. , University of Ottawa, 2009.

[34] R. Daviau, A. Khan, E. Lisicka-Skrzek, R. N. Tait, P. Berini, Fabrication of surface plasmon waveguides and integrated components on CYTOP, Vol. 87 ed. , 1914 - 1921: Microelectronics Engineering, 2010.

[35] R. Ulrich and R. Torge, Measurement of Thin Film parameters with a prism coupler, 12 ed. , 2901-2908: Appl. Opto, 1973.

[36] S. Takenobu, Y. Kuwana, Y.S. K. Takayama, M. Ono, H. Sato, N. Keil, W.Brinker, H. Yao, C. Zawadzki, Y. Morizawa and N.Grote, All-polymer 8x8 AWG Wavelength Router using Ultra LowLoss Polymer Optical Waveguide Material (CYTOPTM, Optical Society of America, 2007.

[37] A. Subramanian, J. Irudayaraj and T. Ryan , A mixed self-assembled monolayer-based surface Plasmon immunosensor for detection of E. coli O157:H7, Vol. 21 ed. , 996-1006: Biosensors and Bioelectronics, 2006.

[38] H. T. Gret, Bioconjugate Techniques, 2 ed. , Chap. II (3): Academic Press, 2008.

[39] A. Khan, O. Krupin, E.Lisicka-Skrzek and P.Berini, Sensing of bacteria immobilised under static conditions using long-range surface plasmon waveguides in Cytop, Proc.SPIE8007 ed. , Photonics North , 2011.

[40] Skoog, D.A., F.J. Holler, and S.R. Crouch, Principles of Instrumental Analysis, 6 ed. , Belmont, CA: Thomson Higher Education, 2007.